2011

Gas Phase Laser Synthesis And Processing Of Calcium Phosphate Nanoparticles For Biomedical Applications

Parimal Vilas Bapat
University of Alabama at Birmingham

Recommended Citation

Bapat, Parimal Vilas, "Gas Phase Laser Synthesis And Processing Of Calcium Phosphate Nanoparticles For Biomedical Applications" (2011). *All ETDs from UAB*. 1102.
https://digitalcommons.library.uab.edu/etd-collection/1102

GAS PHASE LASER SYNTHESIS AND PROCESSING OF CALCIUM PHOSPHATE NANOPARTICLES FOR BIOMEDICAL APPLICATIONS

by

PARIMAL V. BAPAT

RENATO P. CAMATA, COMMITTEE CHAIR
SUSAN L. BELLIS
S. AARON CATLEDGE
DERRICK R. DEAN
YOGESH K. VOHRA

A DISSERTATION

Submitted to the graduate faculty of The University of Alabama at Birmingham,
in partial fulfillment of the requirements for the degree of
Doctor of Philosophy

BIRMINGHAM, ALABAMA

2011

GAS PHASE LASER SYNTHESIS AND PROCESSING OF CALCIUM PHOSPHATE NANOPARTICLES FOR BIOMEDICAL APPLICATIONS

PARIMAL V. BAPAT

PHYSICS

ABSTRACT

Biochemical processes make pervasive use of calcium and phosphate ions. Calcium phosphate salts that are naturally nontoxic and bioactive have been used for several medical applications in form of coatings and micropowders. Nanoparticle-based calcium phosphates have been shown to be internalized by living cells and be effective in DNA transfection, drug delivery, and transport of fluorophores for imaging of intracellular processes. They are also expected to interact strongly with cell adhesive proteins and are therefore promising elements in approaches to mimic the complex environment of the extra cellular matrix of bone. Harnessing this biomedical potential requires the ability to control the numerous characteristics of nanophase calcium phosphates that affect biological response, including nanoparticle chemical composition, crystal phase, crystallinity, crystallographic orientation of exposed faces, size, shape, surface area, number concentration, and degree of aggregation. This dissertation focuses on the use of laser-induced gas-phase synthesis for creation of calcium phosphate nanoparticles, and corresponding nanoparticle-based substrates that could offer new opportunities for guiding biological responses through well-controlled biochemical and topological cues.

Gas-phase synthesis of nanoparticles has several characteristics that could enhance control over particle morphology, crystallinity, and surface area, compared to liquid-phase techniques. Synthesis from gas-phase precursors can be carried out at high temperatures and in high-purity inert or reactive gas backgrounds, enabling good control of chemistry, crystal structure, and purity. Moreover, the particle mean free path and number concentration can be controlled independently. This allows regulation of inter-particle collision rates, which can be adjusted to limit aggregation. High-temperature synthesis of well-separated particles is therefore possible. In this work high power lasers are employed to vaporize microcrystalline calcium phosphate materials to generate an aerosol of nanoparticles which is further processed and deposited using principles of aerosol mechanics.

Particles and resulting particle-based systems are analyzed by transmission electron microscopy, atomic force microscopy, X-ray diffraction, and optical absorption. Obtained substrates are functionalized with cell adhesive peptides. Findings show that laser-induced gas-phase synthesis provides attractive new dimensions in the controlled fabrication of calcium phosphate nanoparticles, including manipulation not only of size and chemical composition, but also crystal phase make-up, fractal structure, and nanotopography of derived substrates.

DEDICATION

I dedicate this work to my parents and my girlfriend Ketaki who have always supported me.

ACKNOWLEDGEMENTS

I would like to thank my advisor Dr. Renato P. Camata for everything he has done for me as a graduate mentor. I am grateful for his guidance, support, encouragement and patience he has given me throughout my years of graduate study. I am privileged to have developed as a researcher under his leadership. I must thank Dr. Yogesh K. Vohra for his constant support as my research committee member as well as being our graduate program director. I particularly enjoyed his lectures on solid state physics. I would also like to extend my gratitude towards my research committee members Dr. Aaron S. Catledge, Dr. Susan L. Bellis, and Dr. Derrick R. Dean for their valuable time and suggestions throughout my research.

I would like to thank Dr. David Shealy, the department chair, and rest of the physics department faculty and staff members. I must thank Jerrie McCurry, Amanda Dickinson and Mark Case for their valuable support. My special thanks to Mr. Jerry Sewell of the physics department machine shop for building my experimental equipment. I also enjoyed my relationship with Dr. Vinoy Thomas who always helped and guided me sometime as a researcher, sometime as a friend.

I would like to thank my lab group members Dr. Jonathan Williams and Dr. Marco Bottino for training me in x-ray diffraction and atomic force microscopy. I would like to thank Finn Perkins for helping me with UV-Vis spectroscopy. I would also like to thank REU student Becky Kraft who helped me in designing and implement my

experimental setup that gave us the best results in this dissertation. Also I would like to thank Bonnie Culpepper for helping me with peptide studies.

I enjoyed the time that I have spent with my colleagues: Dr. Gopi Samudrala, Walter Uhoya, Pramesh Singh, Parul Tyagi, Anitha Armugam, Sonal Singh, Leigh Booth, Sunil Karna and Hadiyah Green. I want to thank all my friends, roommates and particularly my girlfriend, Ketaki More who have always supported me during my graduate studies.

I would like to thank the Alabama Commission on Higher Education for the award of a fellowship from the Graduate Research Scholarship Program. This work was supported by the Brazilian Synchrotron Light Laboratory (LNLS)/Brazilian Biosciences National Laboratory (LNBio) under proposal D12A-XRD1-9943. Authors are thankful to Prof. Daniel Zanetti de Florio, Eduardo Souza Santos, and Pedro Ivo Braun Ferreira for assistance during experiments at LNLS, to Dr. Saulius Drukteinis for assembling the system to control the partial pressure of water, and to Justin T. Marbutt for processing of the AFM data. Instrumentation used in this research was supported by the National Science Foundation under grant number DMR-0116098.

Finally, my deepest gratitude goes to my parents for their unending love, support, encouragement and sacrifices made for my studying and living abroad.

TABLE OF CONTENTS

LIST OF TABLES

Tables *Page*

LIST OF FIGURES

CHAPTER 1

INTRODUCTION

1.1 Background and Motivation

Over the past 50 years, bioceramic materials based on alumina, zirconia, calcium phosphates, and bioactive glasses have made significant contributions to the improvement of human health and the development of the modern health care industry. These ceramics can undergo implantation in the human body without releasing toxic substances or triggering immune reactions [1]. They are used to replace or augment various damaged or diseased portions of the musculoskeletal system. One of the primary purposes of these bioceramics has been to repair or substitute bone tissue [1]. Their biocompatibility, low density, chemical stability and in some cases even high wear resistance, has stimulated robust applied research programs, which in turn have led to impressively successful medical applications. Bioceramic materials are now used in repair and replacement systems for hips, knees, teeth, as well as tendons and ligaments [2, 3]. They are also employed in maxillofacial reconstruction, augmentation and stabilization of the jawbone, in the repair of damage caused by periodontal disease, and in spinal fusion procedures, which can be used to treat a number of spinal degenerative conditions and deformities.

Among bioceramics, calcium phosphates (CaP) have long attracted substantial attention because of their compositional similarity to the mineral phase of bone, which contains vast amounts of crystallites of the CaP known as hydroxyapatite (HA) [4]. Moreover, CaP materials offer the opportunity of tunable bioactivity by the deliberate exploitation of their multiple thermodynamically stable crystal phases. Alpha tricalcium phosphate (α-TCP), for example, is a highly resorbable material, whereas HA presents excellent biochemical exchange with the biological environment while maintaining very good long-term stability. This wide range of dissolution properties has made calcium phosphates a popular family of materials in the burgeoning field of bone tissue engineering, where bioactive scaffolds and substrates that can emulate the environment of the extracellular matrix (ECM) of bone are of paramount importance.

Because calcium phosphates generally exhibit limited mechanical strength and low resistance to fracture and crack growth, most of their applications are in non-load bearing systems. One such application is osteoinductive powders used in spinal fusion procedures [5]. Another area in which calcium phosphates are widely used is in osteoconductive coatings on metallic prosthesis [6]. Most of the orthopedic implants commercially available have a plasma-sprayed HA coating aimed at improving bone growth at the bone-implant interface [7].

Their well-established position as thin coatings for surface modification of metallic implants and substrates for bone tissue engineering, have made calcium phosphates a prime material for explorations in a new frontier in materials for dentistry and medicine: *the nanoscale.* There is a growing appreciation that the already remarkable bioactive properties of calcium phosphates could be exploited even further by controlling and engineering its phases in the nanometric scale. Recent efforts in bioceramics research are therefore focused on improving the physical, chemical, and biological properties of nanostructured calcium phosphates. This trend is only natural because the calcium phosphate content of bone is actually in the form of HA *nanocrystals.* It is this nanophase bioceramic that provides stiffness to bone. The use of nanophase HA in orthopedics and dentistry is therefore considered to be very promising, owing to its dimensional similarity to bone crystals [1]. In addition, nanostructured materials offer a variety of other performance improvement opportunities with respect to their larger size counterparts. Their large surface-to-volume ratio, active surface chemistry, and enhanced dissolution give them exciting prospects in advanced approaches toward bone regeneration and repair [8, 9]. Apart from bone generation applications, nanophase calcium phosphates are also finding promising opportunities in other areas of biomedicine, such as gene transfection [10], drug delivery [11, 12], and intracellular imaging [13].

Accordingly, the goal of this dissertation was to explore new methods of synthesis and processing of nanophase calcium phosphates with the potential to enhance the impact of these materials in medical applications. The focus was on the use of materials physics techniques to produce and characterize these nanophase bioceramics.

1.2 Statement of Dissertation Objectives

The first objective of this dissertation was to study the formation of gas-suspended nanoparticles generated by laser ablation of calcium phosphate materials. Because very few studies have been conducted to date on the characteristics of aerosols produced during laser ablation of calcium phosphates, this first objective was important to establish the most suitable experimental configurations and parameters to achieve efficient particle generation.

Our second objective was to use the general knowledge obtained in calcium-phosphate laser ablation aerosols, to develop and implement a reliable gas-phase method combining laser ablation synthesis and aerosol processing for synthesizing hydroxyapatite nanoparticles with controlled size, degree of aggregation and average interparticle separation as biochemically active substrates. Of great importance for biomedical applications was also the demonstration that these HA nanoparticle-based substrates can be effectively conjugated with relevant biomolecules. We have accomplished this by functionalizing the HA nanoparticles with RGD peptides with polyacidic amino acid domains.

Finally, our third objective was to explore whether laser gas-phase synthesis could be used to produce nanophase calcium phosphate materials with biphasic character. Biphasic calcium phosphate systems in bulk [14] and thin film [15] form have exhibited remarkable enhancement in bioactivity, and our purpose was to investigate if biphasic calcium phosphate configurations can also be obtained in the nanophase.

1.3 Dissertation Outline

Attainment of the stated objectives is pursued beginning in Chapter 2, in which an overview of the fundamental characteristics and biologically relevant properties of calcium phosphates is presented. Our focus is to show that a variety of unexplored research opportunities exist for calcium phosphate nanoparticles both, in the form of nanopowders and nanostructured surfaces with controlled nanoscale topography and chemical composition.

Chapter 3 then presents our general approach for nanoparticle generation by laser ablation in the gas phase, highlighting the physical processes involved in particle formation as well as subsequent processing and manipulation. The general characteristics of aerosols produced during calcium phosphate ablation and the techniques use for nanoparticle characterization are reviewed.

In Chapter 4, we show how the general synthesis and processing principles discussed in Chapter 3 have been applied to the production of a variety of nanoparticles during ablation of calcium phosphate materials. These particles range from fractal-like, to spherically compact, to irregularly-shape structures. The interesting effects of laser energy density as well as total pressure on the particle morphology are discussed in the context of the fluid transport properties of the aerosol reactor used.

The explorations of Chapter 4 and the finessing of the synthesis configuration leads to substantial control achieved in the nanoparticle synthesis reported in Chapter 5. Here we show how nanoparticles of one of the most important calcium phosphate phases (HA) can be synthesized using laser/aerosol processing and deposited with good control and very low degree of aggregation. Substrates with well-defined nanotopography are hence produced. Similar substrates are evaluated for peptide attachment and show potential for use in cell biology studies aimed at decoupling the effects of nanotopography and surface chemistry on the behavior of osteoprecursor cells.

Combining the nanophase characteristics of the calcium phosphates produced here with the ease that this material manifests a variety of bioactive crystallographic phases, represents an opportunity of great potential. In an effort to seize on this potential, we describe in Chapter 6 evidence that gas-phase laser aerosol synthesis may indeed be able to produce biphasic nanophase material, which could be an exciting new class of nanophase bioceramics with tailored bioactivity for specific applications.

Chapter 7 reviews the overall conclusions of the research. Chapters 8 and 9 close the dissertation with some prospects for future work in the area and a list of presentations and publications associated with this document.

CHAPTER 2

CALCIUM PHOSPHATE BIOCERAMICS AND NANOPARTICLES

2.1 Introduction

Calcium phosphates (CaP) represent a family of materials containing calcium ions (Ca^{2+}), phosphate groups (PO_4^{3-}), and occasionally hydrogen and hydroxyl groups (OH^-). They are thus composed of ions commonly found in the physiological environment, which makes them highly biocompatible. Numerous such compounds are thermodynamically stable in a variety of crystallographic configurations including hydroxyapatite [$Ca_{10}(PO_4)_6(OH)_2$, HA], tricalcium phosphate [$Ca_3(PO_4)_2$, α-TCP and β-TCP], tetracalcium phosphate [$Ca_4(PO_4)_2O$, TTCP], octacalcium phosphate [$Ca_8H_2(PO_4)_6 \cdot 5H_2O$, OCP], dicalcium phosphate dihydrate [$CaHPO_4 \cdot 2H_2O$, DCPD], and dicalcium phosphate anhydrous [$CaHPO_4$, DCPA]. Amorphous materials with stoichiometry similar to these crystalline compounds may also form under conditions far from thermodynamic equilibrium (e.g., amorphous hydroxyapatite: a-HA). These compounds typically differ in their Ca/P molar ratio and exhibit dramatically different kinetics of dissolution in aqueous media. Consequently, different phases are used in different applications depending on the desired degree of bioactivity and resorbability. Because Ca^{2+} and PO_4^{3-} ions play important roles in a variety of key biochemical processes such as cell signaling, regulation of gene expression, protein and nucleic acid synthesis, and cellular metabolism, all calcium phosphate compounds interact with life at very basic levels [16, 17]. Therefore, they have long been the focal point of much research attention in biomaterials. The goal of this chapter is to provide an overview of the fundamental properties of various calcium phosphate materials and how these compounds are now being synthesized in the form of nanoparticles by a great variety of routes. Also discussed are the main aspects of their interaction with biological systems which point to numerous open-ended research opportunities in biomaterials.

2.2 Fundamental Characteristics of Calcium Phosphate Bioceramics

Hydroxyapatite

HA is classified along the apatitic minerals. These crystals correspond to phosphate-based materials with the formula $Ca_5(PO_4)_3X$, where X can be F, Cl, OH, or a mixture thereof. In the case of HA one has X = OH. Crystalline HA is found in large proportions in mammalian bones and teeth providing these tissues with their structural rigidity. Most of the biological apatites are calcium-deficient and have Ca/P ratio in the 1.62-1.65 range. Ca/P ratio of an idealized HA system would be 1.67. HA crystallizes in a hexagonal lattice structure ($P6_3/m$ space group) with lattice parameters $a = b = 9.432$ Å and $c = 6.881$ Å. Hexagons of Ca^{2+} ions are surrounded by hexagons of PO_4^{3-} ions, as depicted in Fig. 1. These hexagonal arrays are built on one another along the c-axis of the crystal. Four additional Ca^{2+} ions are arranged between the hexagons along the c-axis, and two hydroxyl (OH^-) groups lie in the center of the hexagon along the *c*-axis [18]. Among all the unsubstituted calcium phosphate compounds, HA is the most stable phase in the physiological condition of pH ~ 7.4. HA has a melting point of 1570°C. Around 1300°C, HA starts to decompose into TCP or TTCP at ambient pressure. Electrically, HA is an insula tor with $E_g \sim 4.51$ eV [19, 20]. Because of its relative insolubility, biocompatibility and osteoconductivity, HA continues to be sought and used as a promising material for bone tissue regeneration applications [1].

Tricalcium Phosphate

Tricalcium phosphate is another form of calcium phosphate which is widely used in clinical applications mainly because of its resorbable properties. TCP has the chemical formula $Ca_3(PO_4)_2$ which gives a Ca/P ratio of 1.5. There are two crystalline forms of TCP: α-TCP and β-TCP. α-TCP has a monoclinic structure (space group $P2_1/a$) with lattice parameters $a = 12.887$ Å, $b = 27.280$ Å, $c = 15.219$ Å, and $\beta = 126.20°$ [21], while β-TCP also known as β-whitlockite has a rhombohedral structure (space group $R3c$) with $a = 10.439$ Å and $c = 37.375$ Å [22]. The relatively high solubility and high bioactivity of TCP makes it an obvious choice for developing biphasic composites that combine TCP with HA to form partially resorbable scaffolds and bone fillers [13].

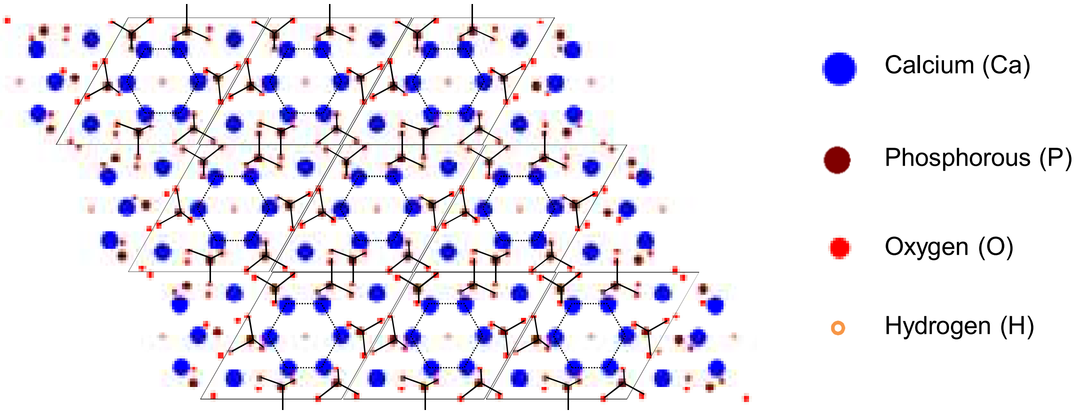

Fig. 1 – Crystal structure of hydroxyapatite. Projection along the (001) direction of the hexagonal structure. In this projection the *c*-axis of the crystal is normal to the surface of the page.

Tetracalcium Phosphate

TTCP is another resorbable mineral from the calcium phosphate family which has shown promise for developing biphasic calcium phosphate composites. The chemical formula for TTCP is $Ca_4(PO_4)_2O$ and it has a Ca/P ratio of 2. TTCP also has a monoclinic structure ($P2_1$ space group) with lattice parameters a = 7.023 Å, b = 11.986 Å, c = 9.473 Å, and β = 90.90° [23]. As shown in Fig. 2, the Ca^{2+} ions and PO_4^{3-} ions are located in planes perpendicular to the b-axis. Each plane contains two Ca-PO_4 columns and one Ca-Ca column. Two adjacent planes in TTCP form a layer that is closely related to that of the apatite structure. TTCP has now been used for many clinical applications pertaining to bone repair and regeneration [24].

Octacalcium phosphate

OCP has a triclinic crystal structure with lattice parameters a = 19.692 Å, b = 9.523 Å, c = 6.835 Å, α = 90.15°, β = 92.54°, and γ = 108.65° [25]. The molar ratio of Ca/P in OCP is 1.33.The crystal structure of OCP exhibits apatite layers that are very analogous to HA, and hydrated layers alternate along c-axis. OCP is usually stable in weak acidic or neutral solutions and has been identified as one of the calcium phosphates that participate in the early stage of biomineralization of calcified tissues [26]. Studies involving OCP have provided insight into the biomineralization processes and OCP might be considered as a starting material for transformation to biological apatite by bio-mimetic approaches.

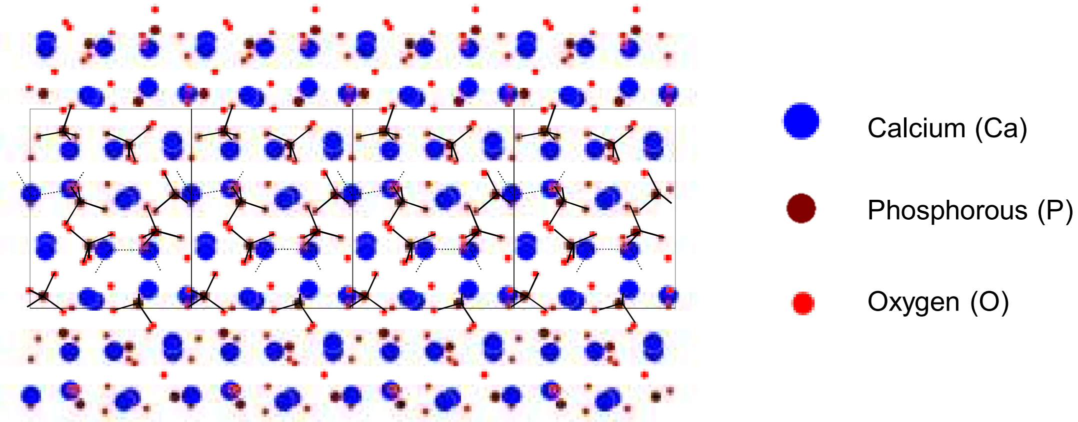

Fig. 2 – Crystal structure of tetracalcium phosphate. Projection along the (001) direction of the monoclinic structure. In this projection the *a*-axis of the structure is normal to the page.

Dicalcium Phosphate

DCP comes in two forms. One is known as Dicalcium phosphate dihydrate (DCPD) and the other as Dicalcium Phosphate Anhydrous (DCPA). DCPD is also known as calcium monohydrogen phosphate or *brushite*, and is believed to be one of the calcium phosphate precursors in the formation of apatite during biomineralization, along with OCP and amorphous calcium phosphate (ACP). DCPD which has a chemical formula $CaHPO_4 \cdot 2H_2O$ has a monoclinic structure (space group *Ia*) with lattice parameters a = 5.812 Å, b = 15.180 Å, c = 6.239 Å, and β = 116.42° [27]. The Ca/P molar ratio of DCPD is 1 and has been commonly used as a starting material for calcium phosphate cement, combined with TTCP.

DCPA, also known as *monetite*, has a triclinic structure (space group *P*1) with lattice parameters a = 6.910 Å, b = 6.627 Å, c = 6.998 Å, α = 96.34°, β = 103.82°, and γ = 88.33° [28]. The Ca/P molar ratio of DCPA is also 1 and the compound exhibits relatively high solubility among the resorbable calcium phosphates.

Dissolution Behavior

One of the most important properties of this family of calcium phosphate compounds is their varying kinetics of dissolution. Amorphous calcium phosphate phases (e.g., a-HA) dissolve very rapidly while the other compounds exhibit slower kinetics of dissolution in the following order: a-HA > DCPA >> TTCP > α-TCP > β-TCP >> HA [29]. Table I shows the solubility product constant, K_{sp}, and Ca/P molar ratio of these calcium phosphate compounds. The broad range of values of K_{sp} observed in these materials leads to patterns of bioactivity and resorbability that are quite different for the various phases. Herein lies the central criterion in selecting the appropriate phase of calcium phosphate for a given application: whether a resorbable or nonresorbable phase is desired, and the resorbability time constant most suitable for the context at hand.

Table I – The solubility product constant, K_{sp}, and the Ca/P molar ratio of calcium phosphate compounds.

Calcium Phosphates	**Crystal Structure**	**Chemical formula**	**Ca/P ratio**	K_{sp}
Hydroxyapatite	Hexagonal	$Ca_5(PO_4)_3(OH)$	1.67	1.59×10^{-117}
Tetracalcium Phosphate	Monoclinic	$Ca_4(PO_4)_2O$	2	1.0×10^{-44}
α-tricalcium phosphate	Monoclinic	$Ca_3O_8P_2$	1.5	3.16×10^{-26}
β-tricalcium phosphate	Rhombohedral	$Ca_3O_8P_2$	1.5	2.83×10^{-30}
Dicalcium phosphate dihydrate	Monoclinic	$CaHPO_4 \cdot 2H_2O$	1	2.04×10^{-7}
Dicalcium phosphate anhydrous	Triclinic	$CaHPO_4$	1	1.26×10^{-7}
Octacalciumphosphate	Triclinic	$Ca_8H_2(PO_4)_65H_2O$	1.33	2.51×10^{-97}

2.3 Calcium Phosphate Bioceramics in the Form of Nanoparticles

The well-established dissolution properties of the various CaP phases discussed in the previous subsection are now being overlaid with a new degree of freedom in calcium phosphate research, namely, the control of CaP materials at the nanoscale. Specifically, CaP nanoparticles both, in amorphous and crystalline phases, have been attracting considerable research interest recently [10, 30, 31]. Part of the original research interest in these nanoparticles was undoubtedly motivated by the already mentioned role that natural CaP nanostructures play in biological processes. The extra cellular matrix (ECM) of bone, for example, contains large amounts of nanocrystals of the calcium phosphate HA [17]. It is therefore not surprising that novel bone regeneration approaches have begun to incorporate nanophase HA in their protocols [8]. It is now widely recognized, however, that CaP nanoparticles provide a stimulating research area for a number of other fundamental and practical reasons. Compared to their corresponding bulk phases, CaP nanoparticles exhibit enhanced dissolution properties [30], improved bioresorbability [32] and superior bioactivity [33]. Their high level of biocompatibility and their nanoscale dimensions, have enabled the successful use of CaP nanoparticles in drug delivery [34], gene transfection [35], intracellular imaging [36, 37] and bone tissue regeneration [38-40]. In all these applications, there is growing appreciation that numerous characteristics of CaP-based nanoparticles (e.g., size, shape, crystal phase, crystallinity, number concentration, degree of aggregation) may be useful to guide biological responses through chemical, topological, mechanical, and even electrical cues [41]. A case in point is the enhanced bioactivity of HA nanoparticles of decreased crystallinity [33].

Achieving nanophase calcium phosphate materials with well-controlled properties is far from trivial, and substantial research energy has been devoted to materials fabrication efforts. Accordingly, numerous solution-based methods have been reported for the synthesis of calcium phosphate nanoparticles including sol-gel synthesis [42, 43], chemical precipitation [32, 44, 45], microemulsion [46-49] and micelle strategies [50, 51], particle formation in organic templates [52-57], and a variety of other wet chemistry approaches [58-63]. Synthesis of CaP nanoparticles by combustion of calcium and phosphate-containing precursors in a flame spray reactor has also been reported [64]. Common challenges faced by these methods are particle aggregation upon precipitation and presence of metastable phases in the final product. One of the motivations for this dissertation work is to contribute to improved control in CaP nanoparticle synthesis with the goal of accelerating the delivery of important advantages associated with use of CaP in the nanophase.

2.4 Interaction of Calcium Phosphate Nanoparticles with Biological Systems

Three aspects of CaP nanoparticles appear to dominate their interaction with biological systems: (i) ionic interactions of constituent anions or cations with key biomolecules; (ii) kinetics of dissolution; and (iii) covalent or hydrogen bonding interactions between crystal-bonded atoms and relevant biomolecules.

Perhaps the most forceful example of the strong positive interaction between nanophase CaP and biological systems is the uptake by living cells of plasmid DNA conjugated to CaP [65]. As shown in Fig. 3, the strong electrostatic incompatibility of DNA and the cell membrane is overcome by the “chemical cloaking” effect achieved by ionic

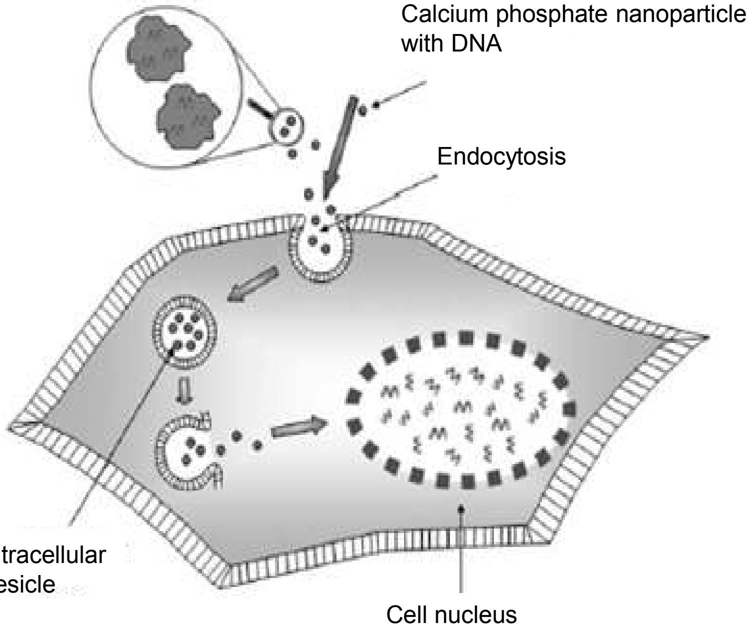

Fig. 3 – Illustration of cellular uptake of genetic material enabled by plasmid DNA conjugation with calcium phosphate nanoparticles.

Note: Adapted from "Transfection of cells with custom-made calcium phosphate nanoparticles coated with DNA" by T. Welzel, I. Radtke, W. Meyer-Zaika, R. Heumannb and M. Epple, 2004, *Journal of Materials Chemistry,* 14, p. 2213 – 2217. Copyright 2004 by Royal Society of Chemistry. Reprinted with permission.

interactions in the co-precipitation of plasmid DNA and CaP. Ca^{2+} ions interact strongly with the phosphate groups in the DNA double helix to form an intimate conjugate that permits seamless cell uptake of genetic material by endocytosis. After intracellular traffic whose details are not yet fully understood, the genetic material finds its way to the nucleus. Reporter genes that lead to expression of fluorescent proteins consistently document successful gene transfection by this route. Having been explored for several decades as one of the most popular non-viral gene vectors [65], CaP materials in the form of nanoparticles are now the basis for very sophisticated gene transfection reagents [10].

Another demonstration of the positive interaction of CaP with biological environments is its general success in platforms for drug delivery [11, 12]. The demand for "miniaturization" of drug carriers to overcome natural barriers in the human circulatory systems and the need for minimum toxicity are well met by nanoscale CaP carriers. CaP nanoparticles also match the reduced size scale that is now aimed in poorly water-soluble drugs to accelerate absorption and transport efficiency. This trend results from the fact that the solubility and dissolution rate of a drug can be increased by reducing the particle size to increase the interfacial surface area. CaP nanoparticles may allow the creation of smart drug carriers for both, controlled drug release timed with the CaP dissolution time constant and ultrasensitive diagnostics in optically tagged particles [66]. Similarly to many systems that are currently being investigated for use as drug delivery agents (e.g., micelles, vesicles, polymers, microspheres, hydrogels) [9], CaP nanoparticles with tunable phase composition and thus adjustable resorption rate can offer an advantage of increasing the efficiency and local character of the drug delivery as well as a controlled release over time. As discussed in the case of gene transfection, CaP particles can cross the cell membrane and deliver drugs to the interior of the cell, which is an important drug delivery modality under investigation in molecular therapy strategies [67]. Finally, one could conceive of CaP nanoparticles doped with magnetic elements that could enable their guiding to targeted area in the organism by means of an external magnetic field. These particles could be helpful in both, diagnostics (e.g., imaging by fluorescent CaP nanoparticles) or therapeutics (e.g., drug del ivery)[68].

In addition to ionic conjugation (exploited in gene transfection) and timed dissolution (advantageous in drug delivery), the possibility of covalent and hydrogen-bonding interactions between CaP and molecules that mediate cell attachment processes is another interactive feature of paramount importance in nanophase CaP. Numerous bone-binding proteins contain acidic amino acid domains that have been found to adhere tightly to CaP surfaces, particularly HA. The N-terminus of salivary statherin, for example, contains the DSSEEK acidic motif whose binding to HA may involve hydrogen bonding according to NMR studies [69, 70]. Similar acidic motifs are also present in osteopontin [71], osteonectin [72, 73], bone sialoprotein [74, 75] and dentin phosphoryn [76]. Acidic amino acid sequences isolated from, or mimicking, the bone-binding regions of these proteins have been used to anchor bioactive peptides on inorganic surfaces [77-80]. These sequences include natural HA-binding domains [78, 79], as well as phosphonates [81], polyaspartates[82], and polyglutamates [80]. It is therefore generally accepted that polyacidic amino acid sequences may provide excellent binding strength to CaP nanoparticles. The incorporation of cell adhesive motifs such as RGD (Arg-Gly-Asp) to these CaP binding sequences may create an ideal platform for productive interaction between the inorganic nanoparticles and biological material. This is because the RGD sequence is recognized by about one third of the human integrins [83, 84], a family of transmembrane glycoproteins [85, 86] that mediate cell adhesion processes. RGD is known to be the integrin recognition site within many cell attachment proteins, including vitronectin (VN), fibronectin (FN) and fibrinogen (Fbg) [87].

Accordingly, the use of a polyglutamate sequence (e.g., E_7) incorporated to a synthetic RGD peptide may offer excellent opportunities to study the interaction between CaP nanoparticles and cells. Indeed, recent studies on microcrystalline HA pellets have shown that RGD peptides adsorb to HA surfaces more effectively when conjugated to an E_7 sequence [88]. A similar tethering effect should be expected in the case of CaP nanoparticles. Of particular interest is the fact that CaP nanoparticles are amenable to deposition on a surface, with the possibility of creating decorated surfaces with variable particle concentration and thereby variable concentration of tethering points. Moreover, the growing interest in various CaP phases that are more resorbable than HA calls for investigations of how peptides adsorb to these more dynamic surfaces. RGD peptides conjugated to E_7 segments could potentially be used in combination with resorbable nanophase CaP systems to produce dynamic controlled release systems that incorporate nanotopographical and biochemical cues into ECM mimics.

Recent studies of cell behavior on surfaces patterned with gold nanoparticles and conjugated to RGD peptides show that integrin function, and thereby cell migration and orientation, can be controlled by how adhesive ligands are patterned and spaced on a surface [89, 90]. The elucidation and exploitation of the basic mechanisms through which such chemical and topographical features of a biomaterials surface determine cell behavior represent one of the most important challenges in biomaterials research. One of the motivating factors of this dissertation is to create CaP nanoparticle-based substrates that in combination with peptide and cell biology studies could help elucidate interactions relevant for applications in bone tissue engineering and regeneration.

2.5 Research Needs and Opportunities in Calcium Phosphate Bioceramic Nanoparticles

Within the scope of this dissertation, two main research needs pertaining to CaP nanoparticles can be identified. First, a survey of the current techniques used in CaP nanoparticle synthesis reveals that a significant opportunity remains for developing techniques with improved control of nanoparticle parameters. Second, the complexity and heterogeneity of existing CaP substrates used in cell biology studies calls for more controlled surfaces in which physical parameters could be changed with greater independence to assess their effect on cell behavior. CaP nanoparticle-based substrates offer an intriguing opportunity to advance research in this area. We discuss in what follows these two opportunities in their own turn.

As briefly mentioned in Section 2.3, the synthesis of CaP nanoparticles has been demonstrated by a great variety of techniques. Particular attention has been given to solution-based methods including sol-gel synthesis [42, 43], chemical precipitation [32, 44, 45], microemulsion [46-49] and micelle strategies [50, 51], particle formation in organic templates [52-57], and a variety of other wet chemistry approaches [58-63]. In addition to these solution-based methods, CaP nanoparticles have also been synthesized by physico-chemical transformation approaches such as flame combustion [64], electrospray [91], electrospinning [92], hydrothermal processing [93], spray pyrolysis [94], and mechanochemical processing [95, 96]. Despite this broad variety of synthesis methods, samples of CaP nanoparticles currently synthesized in research laboratories and industry show poor control of key microscopic parameters and are highly heterogenous [40,90]. The control advantages that a given method exhibits in one area is typically offset by some important limitation that severely affects the final nanophase CaP product. In the case of high-temperature methods, for example, there is the important ability to precisely set the stoichiometry of the final product to the Ca/P molar ratio of 1.667, which leads to HA. However, the reaction times are very long and the required annealing temperatures quite high. Although these methods work well for the standard Ca/P molar ratio of 1.667, it is difficult to reproducibly generate other phases. Deviations from the molar ratio of 1.667 leads to extraneous phases such as α-TCP or β-TCP to appear in conjunction with HA at lower values and CaO to form at higher values [62]. This is especially the case when annealing is used in the process, with α-TCP forming at higher temperatures (~1200°C) and β-TCP forming at lower temperature (~900°C). In addition to the difficulty in controlling the phase composition outside the HA set point, high-temperature methods are often poorly suited for producing uniform nanosized particles. Sintering and growth of nanoscale objects are commonly observed leading to micron sized powders [62].

Low temperature methods used in the synthesis of nanoparticulate material typically offer good control of primary particle size. In the case of the important calcium phosphate HA, however, the situation is less than optimal. HA is essentially a non-resorbable material. As surface/interfacial energy of a crystal is indicative of the difficulty of its forming, sparingly soluble salts, such as HA, have, as a rule, higher interfacial free energy values than soluble ones. On the other hand, the interfacial tension is proportional to the size of the critical nucleus upon dissolution/crystallization. This implies large values for the critical nucleus of HA which is also correlated to the slow dissolution/crystallization of this material [38]. Because of this combination of high surface energy and high surface tension, HA synthesized from low temperature solution methods typically exhibits a wide distribution of particle sizes and irregular particle shapes. This heterogeneity is further increased because of aggregation. Since the particle size and shape represent important parameters that define the interaction of CaP materials with the biological environment [97], commonly available CaP nanoparticles lead to results with poor reproducibility. Low temperature methods also frequently result in the presence of transient and metastable phases in the final product. Lack of size and shape control associated to low phase purity make widespread use of CaP particles problematic. Finally, in addition to liquid phase aggregation, solution-synthesized nanoparticles tend to aggregate upon precipitation. Although this problem can be mitigated by the introduction of surfactants in the process, this normally alters the surface properties of the CaP biomaterial, leading to yet another source of variability in the results.

Many studies of cell attachment, differentiation, and proliferation have been carried out on CaP substrates over the past decade. Although these studies have yielded useful insights into the interaction of peptides and cells with the bioceramic surface, the typical heterogeneity of the CaP samples make it difficult to arrive a very definite conclusions [98]. One example are recent investigations of cell adhesion to polycrystalline HA surfaces that have different degrees of crystallographic texture. Results show that surfaces with an oriented distribution of HA grains promote significantly better cell adhesion than randomly oriented surfaces [98, 99]. Textured HA surfaces seem to enable better cell attachment than randomly-oriented HA surfaces [98]. Changes in crystallographic texture, however, are accompanied by changes in a myriad of other CaP parameters including grain size, amount of amorphous phase, amount of secondary CaP phase, surface roughness, grain size shape, among others. This illustrates how difficult it is to determine with certainty which physico-chemical parameter of CaP parameters is responsible for changes in cell behavior. The ability to create CaP substrates comprising nanoparticles of well-defined size, shape, and crystallographic phase on an otherwise bioinert substrate, could allow the elucidation of important phenomena in the interaction of CaP with biological sytems. Careful control of the CaP nanotopography, accomplished via changes in nanoparticle size and concentration could lead to significant changes in integrin activation and consequently altered cell adhesion behavior. Coupling this controlled nanotopography with tethered E_7-RGD peptides and biphasic particles with predictable dissolution behavior could lead to wide-ranging studies on cell-biomaterials interactions in the CaP system.

Development of synthesis methods that exhibit better control over the composition, size and morphology of CaP particles remains an important priority in this CaP nanoparticle research. Likewise, the use of these nanoparticles to create substrates with controlled nanotopographies that are controlled independently of ionic dissolution signals and biochemical cues represent an excellent opportunity to advance knowledge in cell-biomaterials interactions. This dissertation seeks to contribute in these two important areas by first demonstrating techniques for improved controlled of CaP nanoparticle synthesis, and then by the application of these nanoparticles to the creation of 2D substrates suitable for peptide adsorption and cell biology studies.

CHAPTER 3

GAS PHASE LASER SYNTHESIS AND CHARACTERIZATION OF CALCIUM PHOSPHATE NANOPARTICLES

3.1 Introduction

As discussed in the previous chapter, several solution-based methods have been reported for synthesizing CaP nanoparticles [30,40,42,44,48]. Common challenges faced by these methods are particle aggregation upon precipitation and uncontrolled presence of multiple phases in the final product. In contrast with liquid-medium methods, gas-phase synthesis has several characteristics that could enhance control over particle morphology and crystallinity. Synthesis from gas-phase precursors can be carried out at high temperatures and in high-purity gas backgrounds, enabling good control of crystal structure and purity. Moreover, the particle mean free path and number concentration can be controlled independently. This allows regulation of inter-particle collision rates, which can be adjusted to limit aggregation. High-temperature synthesis of well-separated particles is therefore possible, eliminating growth to undesirably large sizes. Despite these attractive features, there have been few studies on gas-phase CaP nanoparticle synthesis due to the high temperature required to produce chemical or physical vapors of CaP precursors. One solution to this problem is the use of high-power lasers to vaporize solid

CaP materials [100]. In this chapter, we describe an approach to generate an aerosol by the laser ablation of a solid HA target which can be further processed using principles of aerosol mechanics and subsequently deposited on solid substrates or suspended in liquid media for characterization. We also discuss the fundamentals of the characterization techniques used in the study of these particles.

3.2 Generation of Nanoparticles in the Gas Phase by Laser Ablation

3.2.1 Basic Physical Phenomena

When a high power pulsed laser beam irradiates a solid target material above a certain power threshold, a substantial amount of target material can be ejected from the irradiated surface. The vaporized material usually forms a plasma plume which consists of ionic species, neutral atoms, electrons, and particulates of the target material. The plume expands outward from the ablated surface. The process can occur in vacuum or in the presence of inert or reactive gas backgrounds. The placement of a substrate in the path of the expanding plume permits the deposition of a thin film material on a substrate of choice. Thin film deposition in this configuration is the basis for the physical vapor technique known as Pulsed Laser Deposition (PLD). This technique offers much flexibility and many advantages in thin film fabrication, not the least of which is the common reproduction of the stoichiometry of complex target materials in the resulting films.

The removal of the deposition substrate used in PLD, and the continuous flow of a carrier gas over the target region, create the conditions for a related but different materials fabrication approach. As illustrated in Fig. 4, the laser plume now interacts only with the atoms in the gas background. For background pressures in the range of 1-760 Torr, collisions with the gas species thermalize the expanding plasma and lead to the nucleation of particles at the edge of the plume. The rapid quenching of the plume vapor allows the synthesis of particles of metastable and little explored materials systems by carefully choosing a target of suitable composition or a powder mixture of appropriate stoichiometry. Moreover, production of high purity final materials can be assured as the high temperature associated with ablation is achieved locally thus reducing the incorporation of contaminants coming from other surfaces in the system. Since particles formed are carried downstream by the flowing gas, the result is a gas-suspended particle population (i.e., an aerosol) that can be processed, deposited on a surface as depicted in Fig. 4, or dispersed in a solution. This principle has proven successful in the synthesis of metallic and semiconductor nanocrystals for a variety of catalytic [101], sensing [102], and optoelectronic applications [103]. In this work we describe how it has been further developed to fabricate CaP nanoparticles.

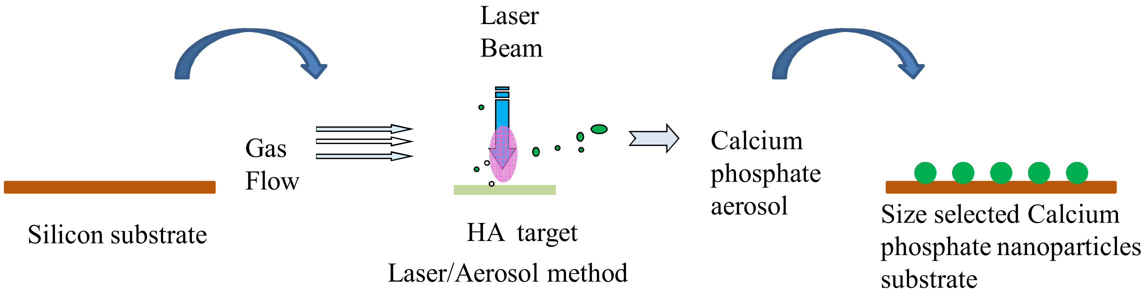

Fig. 4 – Schematic representation of the main processes involved in laser-induced gas-phase calcium phosphate nanoparticle synthesis and the preparation of substrates comprising the corresponding size-selected nanoparticles on bioinert surfaces.

3.2.2 The Aerosol State

Aerosols are suspensions of fine solid particles or liquid droplets in a gas medium. Examples of aerosols include smog, smoke, and clouds. Aerosol methods and techniques have been developed over the past 50 years primarily for studying the behavior of submicron particles that play important roles in atmospheric science [104]. More recently there has been growing interest in adapting these methods to the synthesis and processing of novel nanoparticles [103, 105]. This is mainly due to the fact that aerosol methods have the ability to manipulate the formation, growth, and structuring of nanoparticles in the gas phase. This ability allows aerosol processes to exert significant control over the size, crystal structure, and chemistry of nanoparticles. Various aerosol-based techniques have relied on particle generation by laser ablation [106, 107], spark discharge [108], thermal evaporation [109], and chemical vapors [110]. After generation these particles are typically processed and result in a final particle ensemble in the form of nano powders [111], nanocomposite particulates [112], or nanostructured coatings [113].

Most of the control of the aerosol state is gained by altering the dynamics of the gas-suspended nanoparticle population, which affects the particle number concentration and distribution of sizes. General insight into how this is accomplished can be gained by an inspection of the discrete aerosol General Dynamic Equation [114]. This equation is actually an infinite set of coupled discrete population balance differential equations able to describe, in principle, the dynamics of a system of spherical particles undergoing nucleation from gas-phase molecules, evaporation, condensational growth, and agglomeration [114]:

$$\begin{aligned}\frac{dN(v_1,t)}{dt} &= -N(v_1,t)\sum_{j=1}^{\infty}K(v_1,v_j)N(v_j,t)+\sum_{j=2}^{\infty}(1+\delta_{2,j})E(v_j)N(v_j,t)\\ \frac{dN(v_i,t)}{dt} &= \tfrac{1}{2}\sum_{j=1}^{i-1}K(v_{i-j},v_j)N(v_{i-j},t)N(v_j,t)-N(v_i,t)\sum_{j=1}^{\infty}K(v_i,v_j)N(v_j,t)\\ &\quad +E(v_{i+1})N(v_{i+1},t)-E(v_i)N(v_i,t)\end{aligned}\tag{1}$$

where v_i is the particle volume, and the coefficients $K_{i,j}$ and E_i are the kinetic coefficient of agglomeration and the evaporation coefficient, respectively.

The equation for v_1 represents the net rate of formation of monomers that constitute the particles. The first term in the right-hand side of the v_1 equation gives the collision rate of monomers, which actually gives rise to formation of new particles in the system. The second term in the right-hand side of the same equation accounts for the rate of evaporation of monomers from existing particles, which would represent particle shrinkage. The infinite set of equations for $i > 1$ represent the processes of coagulation growth (first and second terms) as well as condensation (third term) and evaporation (fourth term).

The overall structure of Eq. (1) captures the essential physics of the dynamic behavior of an aerosol population. Vapor supersaturation leads to nucleation. The processes of condensation and evaporation of monomers from nucleated particles then set in and can lead to particle growth or shrinkage depending on the vapor concentration in the environment. Simultaneously to these processes, coagulation growth is also present with its relative importance depending on the number concentration of particles.

When $i >> 1$ these equations can be approximately represented by a system of continuous integro-differential equations. Needless to say, the dynamic equations that result are not analytically solvable except for very simple cases. Numerical solutions in cases that approach realistic conditions are possible taking advantage of computational methods such as Sectional Methods for the Size Distribution [115], Time-Driven Molecular Dynamics Simulations [116], and Monte Carlo Simulations [117], among others.

Guided by these general insights and numerical solutions of Eq. (1) when appropriate, it is possible to control the overall size distribution of the aerosol by altering conditions that lead to nucleation, condensation, and coagulation processes during the evolution of nanoparticle aerosols [114].

Aside from interfering with the dynamic behavior of the entire aerosol population, another effective method for manipulation of an aerosol size distribution has been electrical mobility classification [118]. In this case, the aerosol is fractionated according to size and a specific fraction selected. This approach can lead to new aerosol states with substantially narrower size distributions. Such fractionation is useful in materials fabrication and is described in greater detail in Section 3.3.4.

3.2.3 Dynamics of Calcium Phosphate Nanoparticle Aerosols

When applying the general insights of the General Dynamic Equation [Eq. (1)] to a specific aerosol, it is helpful to possess information about the characteristics of the aerosol generating process. Likewise, for developing a system capable of synthesizing CaP nanoparticles using laser ablation and aerosol processing it is important to understand the essential dynamic behavior of the CaP plume generated by laser ablation, and the size distribution of the ensuing aerosols. Pulsed laser ablation of CaP materials, especially HA, has been widely used for growing biocompatible HA films on titanium implants and is a well-studied phenomenon not only in inert environment but also in water atmosphere [119]. Water atmosphere is known to play an important role in HA film formation [15]. Optical emission spectroscopy of laser ablated HA targets in vacuum reveal that emission is completely dominated by neutral calcium ions with important contribution coming from calcium oxide radicals. Plume consists of three emissive components. Atomic species CaI, CaII, OI and PI are mainly located in the first emissive component of the plume and expand at a velocity of about 2×10^4 m/s [120]. Calcium oxide radicals are found in both components of the plume, expanding at velocities of $7.5\text{x}10^3$ m/s and $2.6\text{x}10^3$ m/s in the first and second components, respectively [120]. Optical emission spectroscopy of laser ablated HA targets in water atmosphere of 0.1-1 mbar show the same general composition of each emissive component, except that some irregularities are observed in the shape of the plume especially at 1 mbar water vapor pressure [119].

3.3 Processing and Deposition of Nanoparticles from the Aerosol State

3.3.1 Temperature Control

Careful temperature control is essential in the synthesis of ceramic materials from the gas phase. Temperature influences the phase composition and the structural quality of the nucleated and growing nanoparticles. Atomic species impinging onto a nanoparticle above the critical size experience diffusion, which is a function of temperature according to

$$D = D_0 \exp\left(-\frac{\Delta E}{k_B T}\right) \tag{2}$$

where D is the diffusion coefficient, D_0 is a constant, ΔE is activation energy for diffusion, k_B is the Boltzmann constant, and T is the temperature. High temperature enhances the surface and bulk diffusion an impinging species, and activates the atomic rearrangement into proper sites of the crystal lattice. Hence the rate of crystallization strongly depends on the nanoparticle temperature. Temperature also determines the heat loss of the condensate to the background gas. In general, the higher the cooling rate of the condensate, the lower the rate of crystallization. Therefore, if the temperature is sufficiently high above a critical point, the cooling rate decreases and the crystallization improves [121].

The most effective way of controlling the temperature during laser aerosol synthesis is by carrying out laser ablation in an independently heated environment, such as a tube furnace. Fig. 5 shows a schematic of the ablation chamber assembled to achieve this purpose in this work. A solid target, in the shape of a circular disk and containing the precursor compound for CaP nanoparticle synthesis, is mounted on a rotating holder inside a 25.4 mm diameter tube furnace. The temperature inside the furnace, to which we refer to as the "ablation chamber", can be adjusted in the 700-900°C range. A continuous flow of a background gas mixture is sustained through the ablation chamber at a total constant pressure of 960 mbar, monitored through a capacitance pressure gauge. Pulses from the focused beam of a KrF excimer laser (248 nm) with energy density of 3-5 J/cm^2 and repetition rate of 1-10 Hz are admitted into the chamber through a UV-transparent window and ablate the target. Nanoparticles generated are entrained in the gas stream forming an ultrafine aerosol. This entire process takes place under a reproducible temperature profile in an attempt to control the crystal character and quality of the produced nanoparticles.

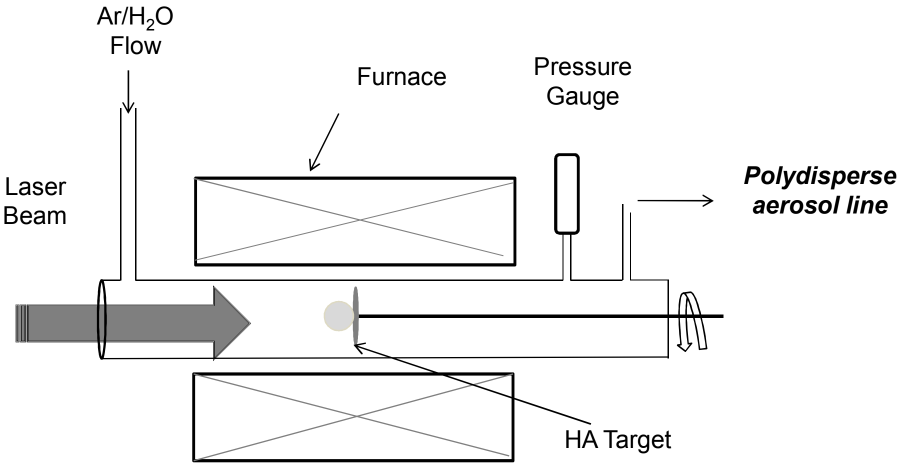

Fig. 5 – Diagram of the ablation chamber used for calcium phosphate nanoparticle generation, featuring a rotating target holder in a tube furnace. The laser beam has access to the chamber through a UV window. A continuous flow of Ar/H_2O is maintained through the chamber.

3.3.2 Synthesis in Reactive Environments

It is a well-known fact that hydroxyl groups (OH^-) play a major role in the crystal quality and phase of CaP materials. It has been shown that atmospheres containing water vapor are highly suitable for growing good quality HA thin films by PLD [122]. Biphasic CaP thin films have also been grown by controlling the OH^- concentration in the environment [15]. It is therefore anticipated that a reactive environment rich in OH^- is also critical for achieving good control in CaP nanoparticle synthesis. This line of reasoning emerges from the understanding that OH^- groups have a much lower probability of incorporation into the growing films or nanoparticles due to their higher diffusivity and reactivity in comparison with other species in the plume. In addition, complex segregation processes within are likely to cause the depletion of OH^- from important areas of particle nucleation and growth. It is in order to compensate this loss of OH^- groups that laser synthesis of CaP materials requires a reactive environment rich in OH^-.

Creating a reactive environment rich in OH^- during nanoparticle production by laser ablation is a relatively straightforward process. This is because laser-induced synthesis is particularly suited for reactive synthesis. The operation of the energy source for the process (i.e., the laser) is independent of the pressure and ambient of the chamber. This is not the case in other methods such as sputtering and spark discharge processes that depend on the ambient constituents for sustaining target bombardment. Because the plasma is produced by energy originating from the external laser, the ablation chamber can be backfilled with virtually any gas-phase chemical species at any pressures ranging from mTorr to ambient with no complicating factors coming into play. In fact, laser synthesis of nanoparticles offers perhaps the broadest dynamic range in terms of pressure and kinds of reactive species that can be employed.

In Fig. 6. we show how a reactive environment with an Ar/H_2O mixture was obtained in the ablation chamber by bubbling a constant flow rate of 500 sccm of Ar gas (99.999% purity) through deionized water kept at a temperature just below the boiling point (flask 1). After removal of excess water by condensation (flask 2), the flow containing water vapor was controllably mixed with pure Ar gas (flask 3) and introduced into the ablation chamber. A hygrometer was used to measure the water content of this mixture (flask 3). The partial pressure of water vapor in the Ar/H_2O mixture was controlled primarily by adjusting the temperature of the deionized water (flask 1) in the range of 30 mbar – 160 mbar. The system used in this dissertation for nanoparticle synthesis has therefore evolved to the point that it features the ability to control both, temperature and OH^- concentration. The temperature and partial pressure of water vapor most fruitful for our investigations were found to be 700-900°C and 30-160 mbar, respectively.

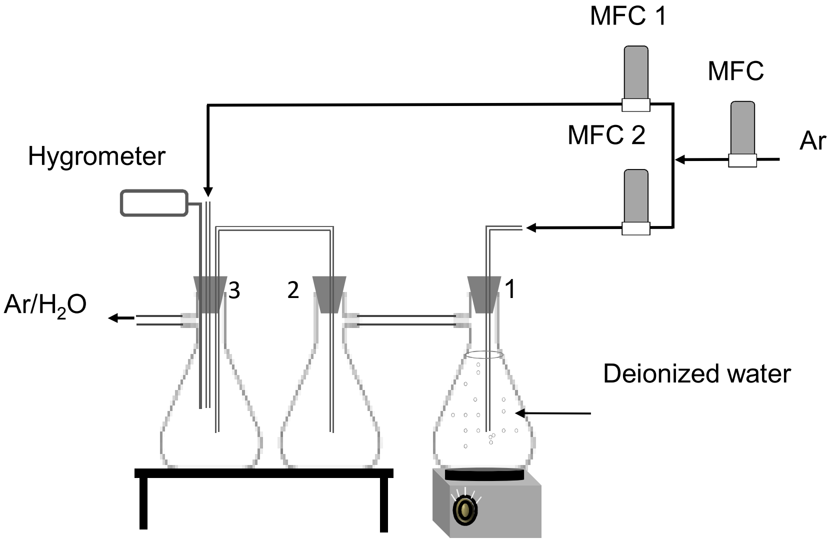

Fig. 6 – Schematic diagram of the apparatus used for creating a controlled Ar/H_2O mixture. MFC, MFC 1, MFC 2 are the mass flow controllers used for monitoring and controlling the Ar gas flow through the chamber.

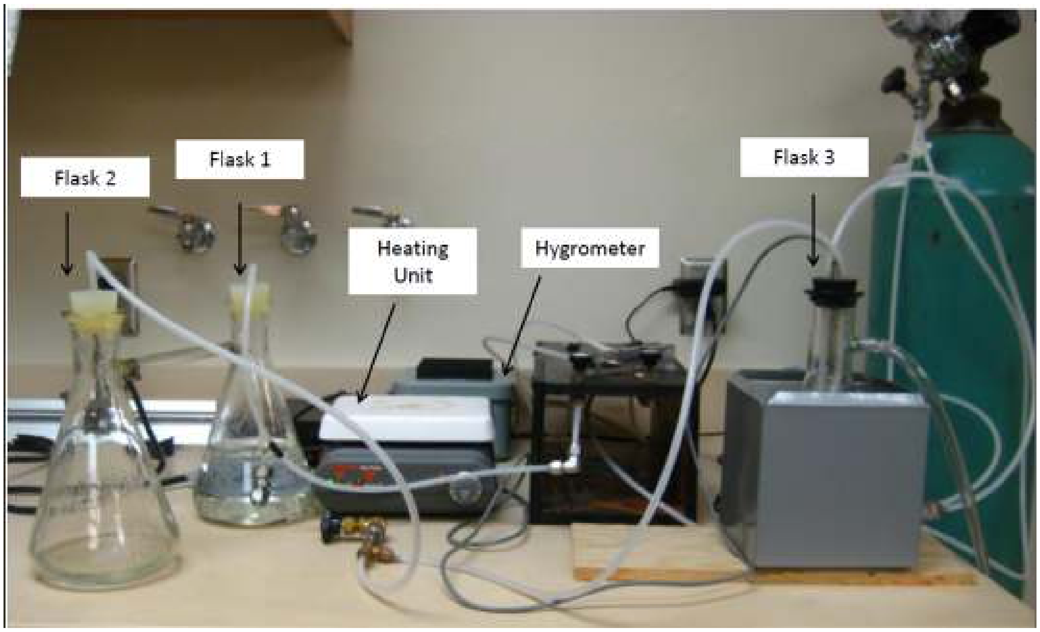

Fig. 7 – Photograph of the apparatus used for creating the controlled Ar/H_2O mixture and shown schematically in Fig. 6.

3.3.3 Charging of Aerosol Nanoparticles

One of the most important characteristics that must be considered during aerosol synthesis of nanoparticles is the electric charge on the nanoparticles. The strength of the Coulomb interaction affects nucleation, condensation growth, and nanoparticle aggregation. In addition, many processing steps in aerosol technology (e.g., mobility classification, electrostatic deposition) use electric fields to manipulate the particles and hence rely on the electric charge on the particles. Monitoring the charge state of the aerosol is therefore absolutely essential in our project since we are using an electrical mobility technique, to be described in the next section, for active size classification. It is well known that for mobility classification to work properly the aerosol as a whole should be approximately neutral and the charge state of the particles should be reasonably well known [118].

Control of the aerosol charge state in materials fabrication approaches is usually accomplished by exposing the aerosol to an equilibrium ion distribution produced within a bipolar diffusion charger. In this process, illustrated in Fig. 8, ambipolar ions are generated using ionizing radiation emitted by radioactive materials in an inert gas ambient. Although this use of diffusion chargers accomplishes both, the neutralization of the aerosol and the elimination of multiply charged particle states, it achieves that at the expense of causing more than 90% of the particles to become neutral. Neutral particles cannot be processed using the DMA, and therefore, this approach usually causes a significant reduction in the throughput of the classified aerosol. Given these facts, achieving high number concentrations of size-selected nanoparticles would seem to require three essential conditions: (i) the total charge state of the aerosol should be close to neutral; (ii) the aerosol should be maximally polarized (i.e., the absolute number of charged particles of either polarity should be as high as possible); and (iii) processing should be carried out at low pressures to minimize time for collisions with walls which cause particle losses.

The use of diffusion charging requires a certain amount of interaction time between ions and nanoparticles, thus setting a lower limit to the operating pressure. Also, long interaction time enhances the possibility of recombination of oppositely charged particles leading to less polarized aerosol. Thus it is apparent that diffusion charging brings substantial limitations to the efficient processing of nanoparticle aerosol.

Fortunately, the generation of nanoparticles by laser ablation creates an opportunity to overcome the limitations of diffusion charging. Because of the highly ionized conditions of the ablation plume, the aerosol formed in laser ablation already exhibits significant charge upon generation. Although the aerosol as a whole can at times be very far from the neutrality condition, which is important for mobility classification, it is generally possible to find experimental conditions that keep the overall charge state to a manageable level. Large numbers of particles exhibit charge in this native state and therefore mobility classification can be successful without the use of diffusion chargers. This is found to significantly increase the throughput of the technique.

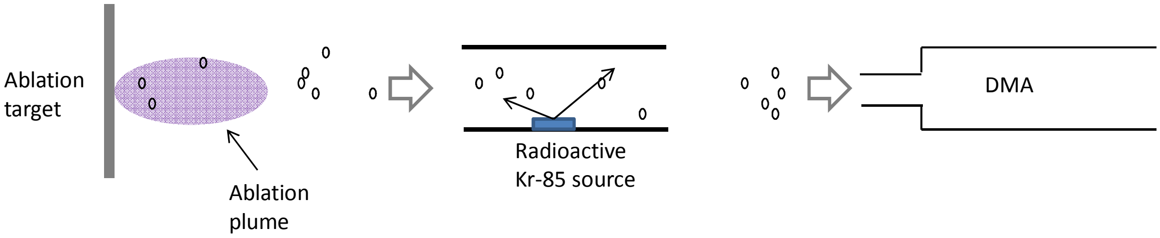

Fig. 8 – Diagram of laser aerosol process showing laser ablation followed by neutralization of the aerosol by a Kr-85 diffusion charger and subsequent flow into the differential mobility analyzer.

3.3.4 Electrical Mobility Classification

One of the most effective methods for manipulation of an aerosol size distribution is fractionated according to size and selection of a specific fraction of choice. This approach can lead to new aerosol states with substantially narrower size distributions. Such fractionation is very useful in materials fabrication. Several approaches involving inertial forces such as hypersonic impaction, aerodynamic lensing, and centrifugation can lead to size fractionation of aerosols. Electrical mobility classification, however, typically achieves the highest resolution. Electrical mobility classification is usually achieved using an instrument known as the Differential Mobility Analyzer (DMA) [118]. The DMA can be regarded as the aerodynamic analog of a dispersive mass spectrometer. As shown in Fig. 9, its most common implementation consists in a coaxial capacitor in which charged nanoparticles from a polydisperse aerosol migrate across a particle-free laminar sheath gas flow due to an applied electric field. The migration velocity of the particles is parallel to the direction of the electric field and is given by

$$\vec{v}_e = Z_p \vec{E} \tag{3}$$

where Z_p is defined as the gas-phase electrical mobility of the particle. A straightforward solution of Newton's law for the Stokes aerodynamic drag force leads to an electrical mobility Z_p given by

$$Z_p = \frac{neC^*}{3\pi\eta D_p} \tag{4}$$

where $ne=q$ is the net charge on the particle, C^* is the slip correction factor that corrects for the granularity of the gas medium at low pressures and small particle sizes, η is the gas kinematic viscosity, and D_p is the aerodynamic diameter of the particle. As it can be

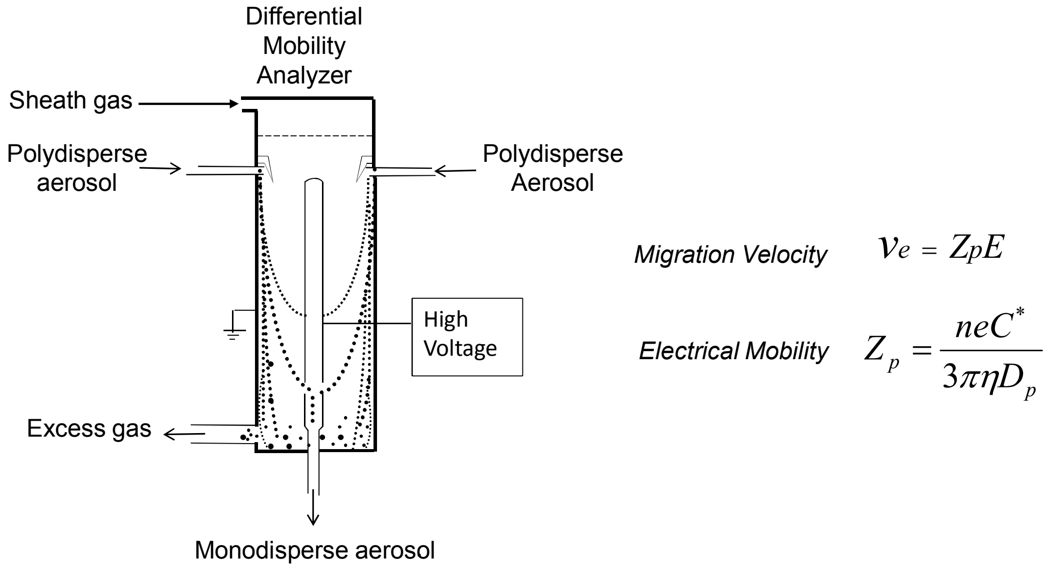

Fig. 9 – Schematic diagram of differential mobility analyzer featuring coaxial capacitor in which charged nanoparticles from a polydisperse aerosol migrate across a particle-free laminar sheath gas flow due to an applied electric field.

surmised from Eq. (4), particles with different diameters D_p move along distinct trajectories as a result of their different electrical mobilities. This effect allows the separation of singly charged particles with respect to size. The presence of particles with multiple charges leads to size distributions with multiple peaks in the classified aerosol, each peak corresponding to a distinct particle charge state. The mobility-classified nanoparticles can then be deposited on a solid substrate using electrostatic precipitation [123], inertial impaction [124], or a combination of both. Thus samples containing nanoparticles of desired chemical composition, size and number concentration can be produced.

3.3.5 Deposition of Aerosol Nanoparticles on Substrates.

Another important aspect of nanoparticle aerosol processing is the efficient deposition of size-classified nanoparticles on substrate. Typically, the deposition of the size classified nanoparticles is carried out in an external collection device coupled to the DMA. Several studies have indicated that the ideal geometry for deposition of size-classified nanoparticles is the nozzle-to-plane electrostatic precipitator configuration [123]. This arrangement can enhance nanoparticle transmission by minimizing the transfer time between classification and deposition.

3.4 Laser Aerosol Synthesis of Calcium Phosphate Nanoparticles

All aspects of particle generation and processing discussed in Sections 3.2 and 3.3 were taken into consideration in developing an integrated process for CaP nanoparticle fabrication. Fig. 10 shows a schematic of the experimental apparatus used in this work. A solid HA target is prepared by compressing a commercial HA powder (97.5% purity, Plasma Biotal Ltd.) at a pressure of 600 psi followed by sintering at 1200°C in Ar/H_2O ambient for 1.5 hours. The target, in the shape of a circular disk, is mounted on a rotating holder inside the 25.4 mm diameter tube furnace described earlier. The temperature inside the furnace can be adjusted in the 700-900°C range. A continuous flow of the Ar/H_2O mixture is sustained through the ablation chamber at a total constant pressure of 960 mbar, monitored through a capacitance pressure gauge. Pulses from the focused beam of a KrF excimer laser (248 nm) with energy density of 3-5 J/cm^2 and repetition rate of 1-10 Hz are admitted into the chamber through a UV-transparent window and ablate the HA target.

Nanoparticles generated are entrained in the gas stream forming an ultrafine aerosol. Due to the highly ionized environment of the ablation plume, the product aerosol consists mostly of charged particles which are then directed to a DMA for mobility classification. The DMA used in these experiments was a Vienna-type instrument [125] with inner and outer electrode diameters of 25 mm and 33 mm, respectively, and classification region of 168 mm. The instrument was operated with an aerosol flow rate of 1 SLM (standard liter per minute) of Ar/H_2O and “sheath” flow rate of 5 SLM of nitrogen. Selection of particles of different mobilities is achieved by applying different voltages to the DMA electrodes. Particles selected within a narrow range of mobilities are extracted from the classification region and deposited on suitable substrates such as transmission electron microscopy (TEM) carbon grids or silicon (Si) substrates in a nozzle-to-plate electrostatic precipitator (0.5 mm nozzle-to-plate separation). In the precipitator, a voltage of –300 V is maintained on the substrate with respect to the deposition nozzle. Alternatively to particle deposition, the number concentration of mobility-classified particles can also be estimated at any time, by diverting the monodisperse aerosol to an electrometer (TSI, Saint Paul, MN, Model 3086A) mounted adjacent to the precipitator. Collection of polydisperse particles is easily accomplished by stopping the sheath flow and grounding the inner electrode. Stable flow conditions and constant total pressure in the system are maintained through the coupled operation of a high-pumping capacity vacuum system, the capacitance vacuum gauge, and various mass flow controllers as shown in Fig. 10.

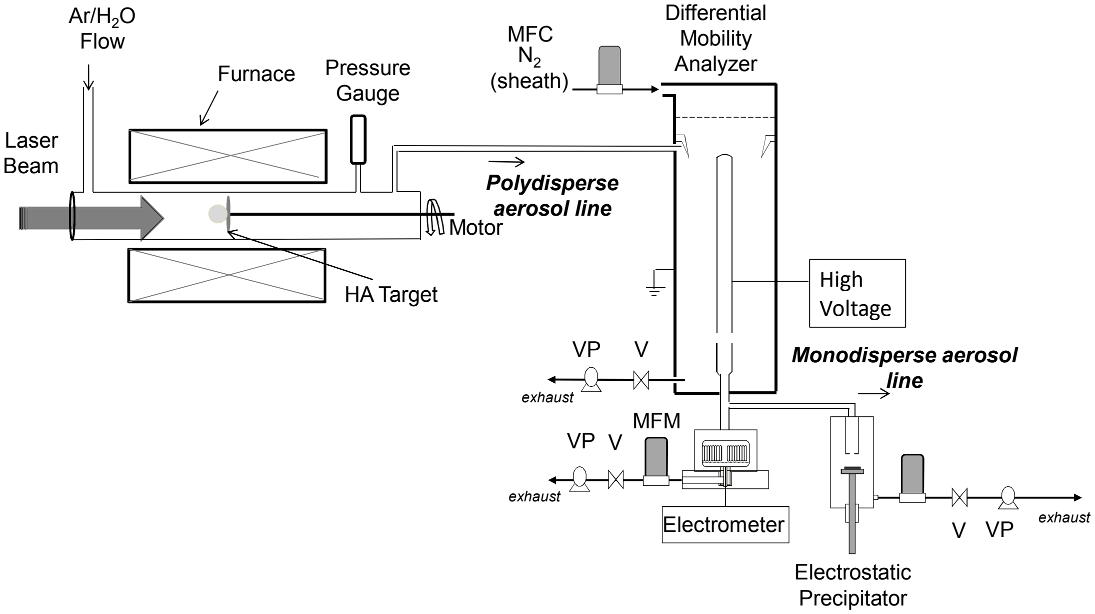

Fig. 10 – Schematic diagram of apparatus used for gas-phase synthesis of calcium phosphate nanoparticles featuring temperature and humidity-controlled ablation chamber, differential mobility analyzer (DMA), electrostatic precipitator, and aerosol electrometer. MFC, MFM, V, and VP refer to mass flow controller, mass flow meter, manual valve, and vacuum pump, respectively.

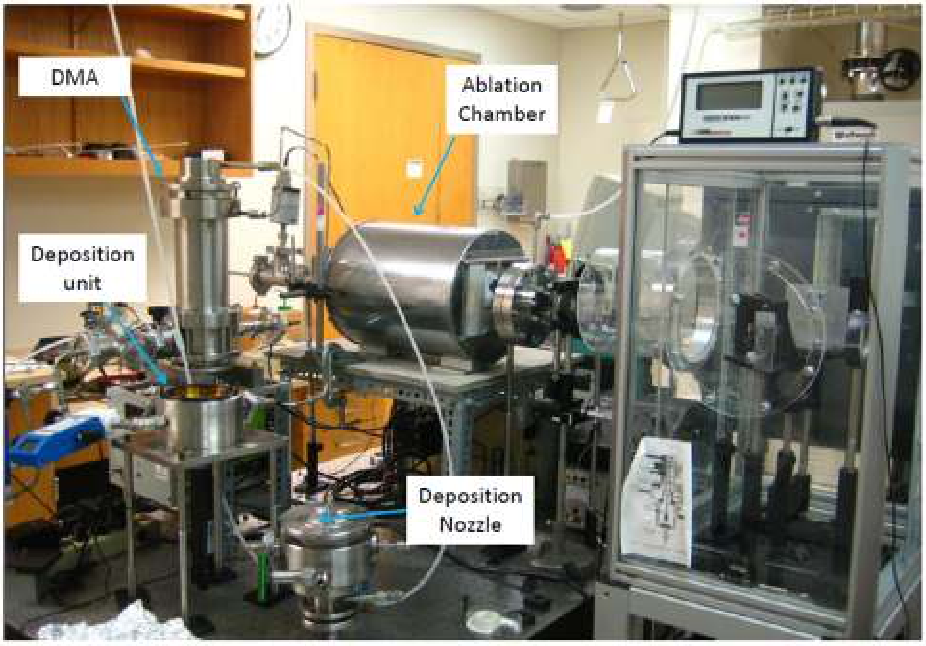

Fig. 11 – Photograph of the apparatus gas-phase laser synthesis shown schematically in Fig. 10 and implemented at UAB in the Center for Nanoscale Materials and Biointegration.

3.5 Characterization of Calcium Phosphate Nanoparticles

In order to characterize the nanoparticles synthesized, we have employed transmission electron microscopy (TEM), atomic force microscopy (AFM), X-ray diffraction (XRD), and optical absorption (OA).

3.5.1 Transmission Electron Microscopy

TEM is a powerful imaging technique that is routinely used in morphological characterization of nanostructured materials. Because the wavelength of a high-energy electron can be significantly smaller than the interatomic spacing in crystals, TEM can be used to image materials with atomic-scale resolution. In this dissertation research, a Tecnai Spirit Twin 20-120 kV (JEOL, Japan) transmission electron microscope was used to determine the morphology and measure the size distribution of nanoparticles deposited directly on holey carbon TEM grids. Samples were imaged under bright field/dark field illumination conditions with an accelerating voltage of 80 kV at magnifications ranging from 2,000× to 20,000×. Images were corrected for condenser and objective astigmatism and acquired using a 1028×1028 charged couple device that captures the impression of the electron beam on a phosphorescent screen. Selected area electron diffraction experiments were also carried out and diffraction patterns for observed deposits recorded. Fig. 12 shows a typical TEM image of nanoparticles produced during laser ablation of an HA target at atmospheric pressure using a laser energy density of ~3 J/cm^2. The particles were deposited on a holey carbon TEM grid with mobility classification set at a 10-nm diameter for singly charged particles.

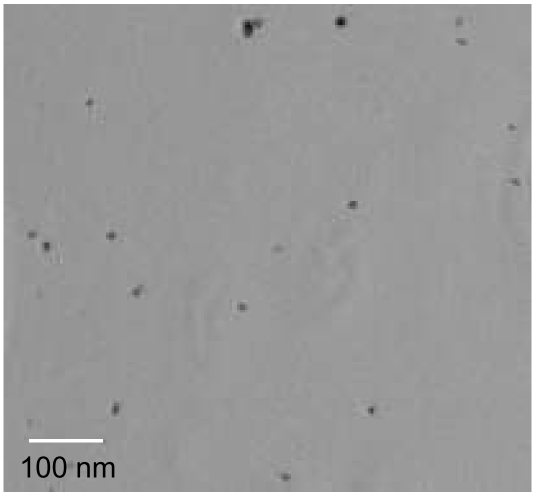

Fig.12 – Transmission electron microscopy (TEM) image of 10 nm calcium phosphate nanoparticles deposited on a TEM grid.

3.5.2 Atomic Force Microscopy

AFM is an imaging technique for probing the surface topography of a sample with a sharp tip attached at the end of a cantilever having a low spring constant. The interaction forces between the tip and the atoms of the scanned surface (order of nN) cause a deflection of the cantilever where the tip is mounted. When there is a change in the surface topography, changes in the cantilever position cause deflections of a laser beam which are detected by an optical lever. The optical lever is operated by reflecting the laser beam off the cantilever. The reflected laser beam strikes a position-sensitive photodetector consisting of two adjacent photodiodes. The differences between the two-photodiode signals indicate the position of the laser spot on the detector and thus the angular deflection of the cantilever. Topographic images with a vertical resolution of the order 0.1 nm can be achieved by scanning over the sample surface and measuring the deflection of the cantilever as a function of the lateral position using the optical lever. This technique allows imaging the samples in air and under liquids. A Nanoscope Dimension 5000 (Digital Instruments, USA) atomic force microscope was used visualize the topography and determine the nanoparticle number concentration as well as size distribution of CaP nanoparticle samples deposited on Si substrates.

Fig. 13 shows AFM scans obtained in contact mode for a sample deposited using a laser energy density of 3 J/cm^2 at a pressure of 720 Torr with size classification aimed at 30 nm. The AFM tip was scanned over a 20 μm × 20 μm area. A uniform distribution of nanoparticles is observed with an estimated number areal density of approximately 2×10^8 cm^{-2}.

The image on the right hand side of Fig. 13 shows a 5 µm × 5 µm scan area of the same sample. This 3D depiction of the sample shows the well separated nanoparticles with an average size near ~30 nm. Fig. 14 shows height profiles obtained from select particles within a similar 5 µm × 5 µm scan area. Three particles denoted by blue, orange and green traces show height profiles with average height of each particle very near 30 nm. These measurements show the ability of the laser-aerosol system to deposit size-controlled nanoparticles.

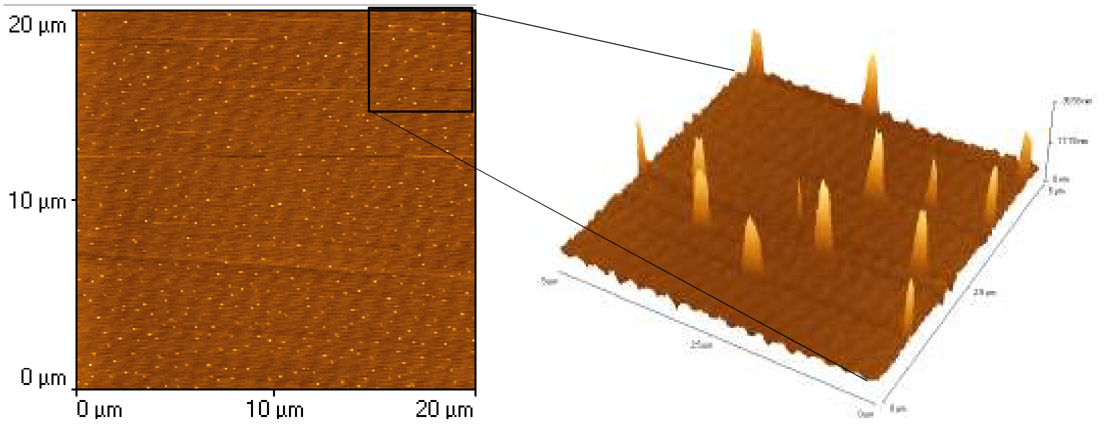

Fig. 13 – Atomic force microscopy scan of well separated 30-nm calcium phosphate nanoparticles deposited on a silicon substrate. Nominal areal number concentration based on deposition time and gas-phase concentration is 2×10^8 cm^{-2}.

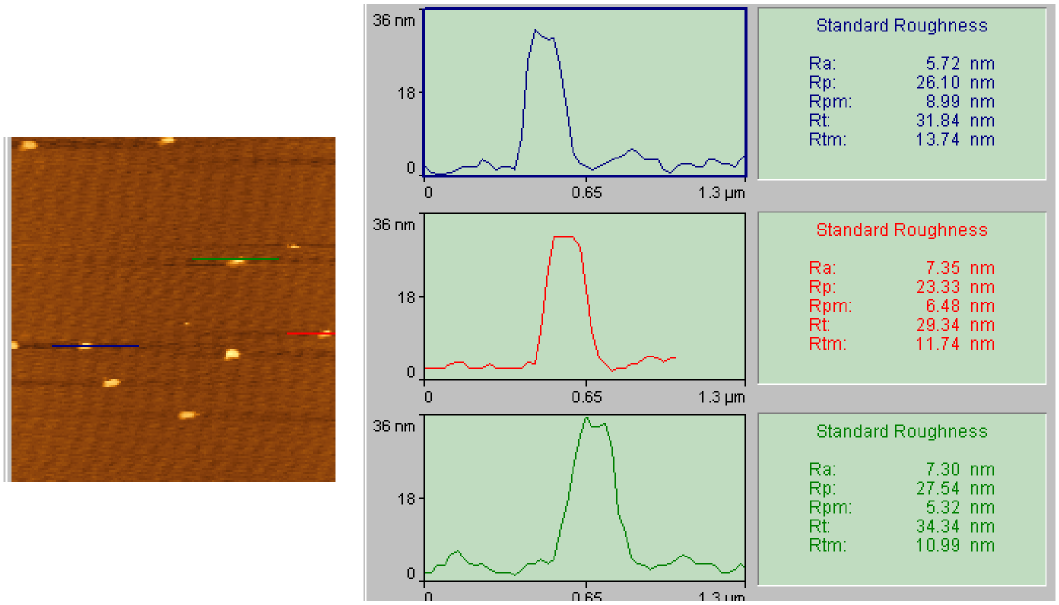

Standard Roughness

Ra: 5.72 nm
Rp: 26.10 nm
Rpm: 8.99 nm
Rt: 31.84 nm
Rtm: 13.74 nm

Standard Roughness

Ra: 7.35 nm
Rp: 23.33 nm
Rpm: 6.48 nm
Rt: 29.34 nm
Rtm: 11.74 nm

Standard Roughness

Ra: 7.30 nm
Rp: 27.54 nm
Rpm: 5.32 nm
Rt: 34.34 nm
Rtm: 10.99 nm

Fig. 14 – Height profiles of select nanoparticles (denoted by Green, Blue and orange lines) obtained from a 5 µm × 5 µm scan area on sample size-selected for 30 nm.

3.5.3 X-ray Diffraction

When a monochromatic X-ray beam with wavelength λ is projected onto a crystalline material at an angle θ, diffraction occurs only when the path difference for the rays coherently scattered from atoms in successive planes is equal to a complete number n of wavelengths. This is known as Bragg's condition, which may be expressed mathematically as

$$2d \sin\theta = n\lambda \quad (n = 1, 2, 3, ...) \tag{5}$$

By varying the angle θ, Bragg's condition is satisfied by different d spacings in crystalline materials. More specifically, for measurement of bulk samples, the conventional θ-2θ scan method is used. The incident X-ray beam strikes a material with varying angle θ and simultaneously the detector generates a diffraction pattern by scanning the angle 2θ. For measurement of thin films or surface deposits, which is the case in this dissertation research, the so-called 2θ scan method is used. In this case, the X-ray beam is made to impinge the sample at a low grazing angle of 1-5°. The detector then produces a diffraction pattern by scanning the angle 2θ. At a grazing angle of incidence, patterns will be dominated by information from the surface. The patterns can be optimized by adjusting the grazing angle of the incident beam.

Particles synthesized in this dissertation research were analyzed by X-ray diffraction (XRD) at UAB using an X'pert diffractometer (Philips, USA) with Cu Kα radiation of 1.5418 Å wavelength and also at the D12A-XRD1 line of the Brazilian Synchrotron Light Laboratory (LNLS) with 8 keV photons (1.5487 Å). The goal of these measurements was to determine the phase composition and crystal structure of the synthesized nanoparticles.

In the UAB thin film X-ray diffractometer, X-rays are produced due to rapid deceleration of thermoelectrons in the Cu tube. The filament in the cathode emits the electrons by heating to high temperatures with an electric current. When the emitted thermoelectrons accelerated by the high voltage strike the anode, X-rays are generated.

At LNLS the X-ray beam is produced by 1.37 GeV electrons injected in the 30-m diameter synchrotron storage ring. Bending of the electron trajectories by electromagnetic fields at suitable locations along the ring leads to emission of X-ray radiation. The convenience of the UAB diffractometer has allowed studies varying several experimental parameters during synthesis, whereas the high brilliance of LNLS allowed observation of details in the diffraction from produced samples that were not apparent in the UAB data.

Fig. 25 (a) shows a typical XRD scan of polydisperse nanoparticles obtained at LNLS. Particles were synthesized at 5 J/cm^2 and 160 mbar of partial pressure of water vapor.

3.5.4 Optical Absorption

By replacing the electrostatic precipitator in the apparatus of Fig. 10 by a simple bubbler, it is possible to disperse the CaP particles produced by laser aerosol synthesis in a liquid medium. This alternative approach to sample generation permits rapid studies of the optical properties of the now *liquid*-suspended nanoparticles. The suspended particles are now obstacles in the path of light rays. They can be studied in relation to their scattering and absorption properties.

When light encounters an obstacle, such as a nanoparticle suspended in one of our liquid samples, the electric charges that compose that obstacle are set into oscillatory motion by the electric field of the electromagnetic wave. Once oscillating, there are two ways the electric charges of the obstacle can return to their ground state. The first is by re-radiating the electromagnetic energy in all directions. This essentially elastic process preserves the wavelength of the incident radiation and is referred to as the *scattering* of light. The second option is to convert the electromagnetic energy into another form, such as thermal energy. This is known as the absorption of light [126]. Both of these processes can yield valuable information for our samples. Scattering is strongly dependent on particle size and can therefore be correlated with particle size distribution and degree of aggregation. Absorption on the other hand is a direct probe of the electronic states in the particles. For select particle samples, we have studied both, scattering and absorption processes in our samples using a Jasco V-530 UV/Vis spectrophotometer with 10-mm Starna quartz spectrophotometer cells. A reference and matching sample were placed in the spectrophotometer and baseline scans were taken prior to optical measurements of the samples of interest. The measurements were taken at a scanning speed of 1000 nm/min with a data pitch of 1.0 nm over a wavelength range from 200 nm to 1100 nm.

3.6 Summary

This chapter has provided a general view of the processes advanced in this dissertation for the synthesis of CaP nanoparticles. Our focus is in employing a laser-induced physical vapor to generate CaP nanoparticles that can then be processed using aerosol techniques. TEM, AFM, XRD, and OA have been described as suitable methods to analyze the samples produced. In the subsequent chapters we show how these methodologies have been applied in the synthesis and characterization of three classes of CaP-based nanoparticles: (i) fractal-like objects with complex shapes; (ii) aggregation-free nearly compact HA nanoparticles; and (iii) CaP nanoparticle samples with evidence of co-existence of several CaP phases.

CHAPTER 4

FRACTAL-LIKE NANOPARTICLES FORMED BY LASER ABLATION OF CALCIUM PHOSPHATE

4.1 Introduction

As discussed in Chapter 3, there are good reasons to suppose that the greatest levels of control in laser/aerosol synthesis of CaP nanoparticles should be achieved at high temperature and with controlled OH-rich reactive environment. Nevertheless, before exploring the effect of these parameters, it is worth investigating nanoparticle generation under the rich interplay offered by laser ablation and aerosol transport. The thermal and non-thermal pathways for relaxation of the energy deposited on the CaP target by the excimer laser, should permit production of a variety of interesting particle morphologies. Likewise, as evidenced by the complex nature of the General Dynamic Equation [Eq. (1)], changes in background pressure and/or processing times could provide different particle characteristics depending on the stage of evolution in which particles are arrested.

Accordingly, we present in this chapter results on particles obtained essentially at room temperature and in inert ambient, for different values of laser energy density and background pressure.

4.2 Synthesis Configuration

For experiments at room temperature and inert ambient, the synthesis configuration was essentially the same as the apparatus shown in Fig. 10. However, the system was operated with no heating and pure Ar in the gas inlet. The pressure in the system was varied in the 80-700 mbar range using the high-pumping capacity vacuum system coupled to the pressure gauge and flow controllers.

4.3 General Nanoparticle Characteristics

Fig. 15 shows a few examples of the variety of particle morphologies that are possible even at room temperature. These particles were obtained using a laser energy density of ~3 J/cm^2. The sample shown in Fig. 15(c) was generated at 200 Torr, whereas the others were produced at ambient pressure. Fig. 15(a) is representative of the varied morphologies that often exist in a single sample. Relatively compact as well as open aggregates, isolated particles, nearly spherical particles as well as particles with tendency to faceting, irregularly shaped particles and aggregates formed of these entities are all observed in this image. Some samples, however, are somewhat more homogeneous, such as the one seen in Fig. 15(b), which is dominated by aggregates, although essentially the same experimental conditions were used. Interestingly, samples have also been observed with very uniform particle morphologies, such as the one shown in Fig. 15(c). In this case, a substantial part of the sample is dominated by compact spherical particles with remarkable diameter uniformity, although smaller, irregular aggregates are also visible in the background. Fig. 15(d) illustrates the size fractionation capability of the experiment, exhibiting particles that were selected by size for 30 nm. Virtually all particles are small aggregates with sizes that agree with this targeted aerodynamic diameter. More importantly, it is clear that mobility classification is capable of removing from the sample all large particles that would otherwise play the dominant role in terms of properties. Despite the rather low level of control, Fig. 15 illustrates the remarkable range of morphologies that are inherent in laser aerosol synthesis of nanoparticles.

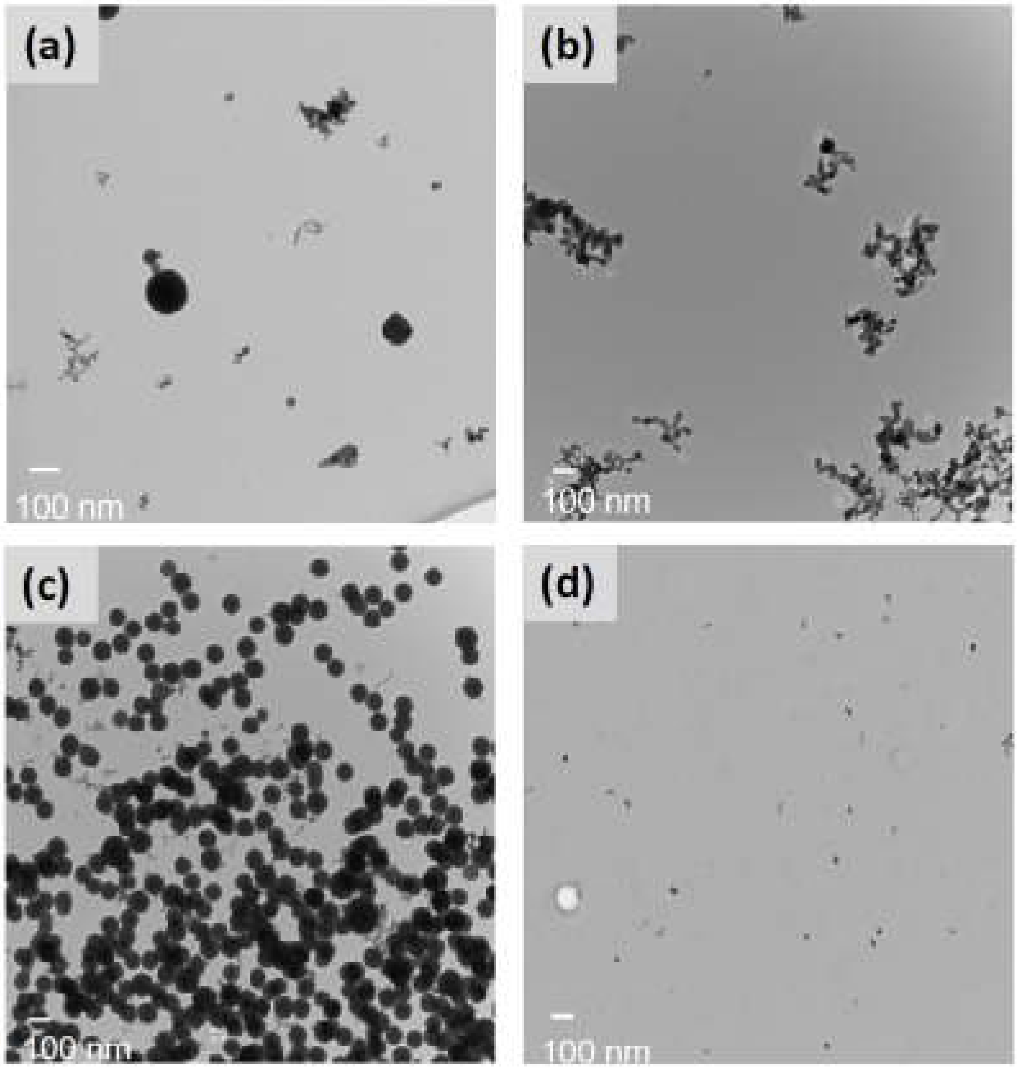

Fig. 15 – Transmission electron microscopy images of nanoparticles generated by laser ablation of hydroxyapatite at room temperature in an inert ambient. The images underscore the variety of nanoparticle morphologies that can be generated using the laser/aerosol method.

4.4 Effect of Laser Energy Density

Fig. 16 seeks to clarify the effect of the two main parameters that can be varied in the room temperature process in inert ambient: (i) the laser energy density; and (ii) background pressure. For all three pressures shown, samples produced at the low energy density value (i.e., 0.3 J/cm^2) are dominated by large particles in the 100-300 nm range. The overall morphology of these particles suggests that they are expelled from the target as molten droplets, as is the case in hydrodynamic sputtering [127]. For the same three pressures, one observes that when the laser energy density is doubled (i.e., 0.6 J/cm^2), comparatively smaller nanoparticle aggregates in the 20-100 nm range become pervasive in the sample. Their irregular shape and small primary particle size indicate that this second particle modality originates from the vapor phase under the higher energy density condition used.

It is apparent therefore that two distinct nanoparticle morphologies exist in the higher energy density samples. Small nanoparticle aggregates (20-100 nm; mostly formed from the vapor phase) along with spherical-like nanoparticles (100-300 nm; molten droplets formed by some thermo-mechanical process).

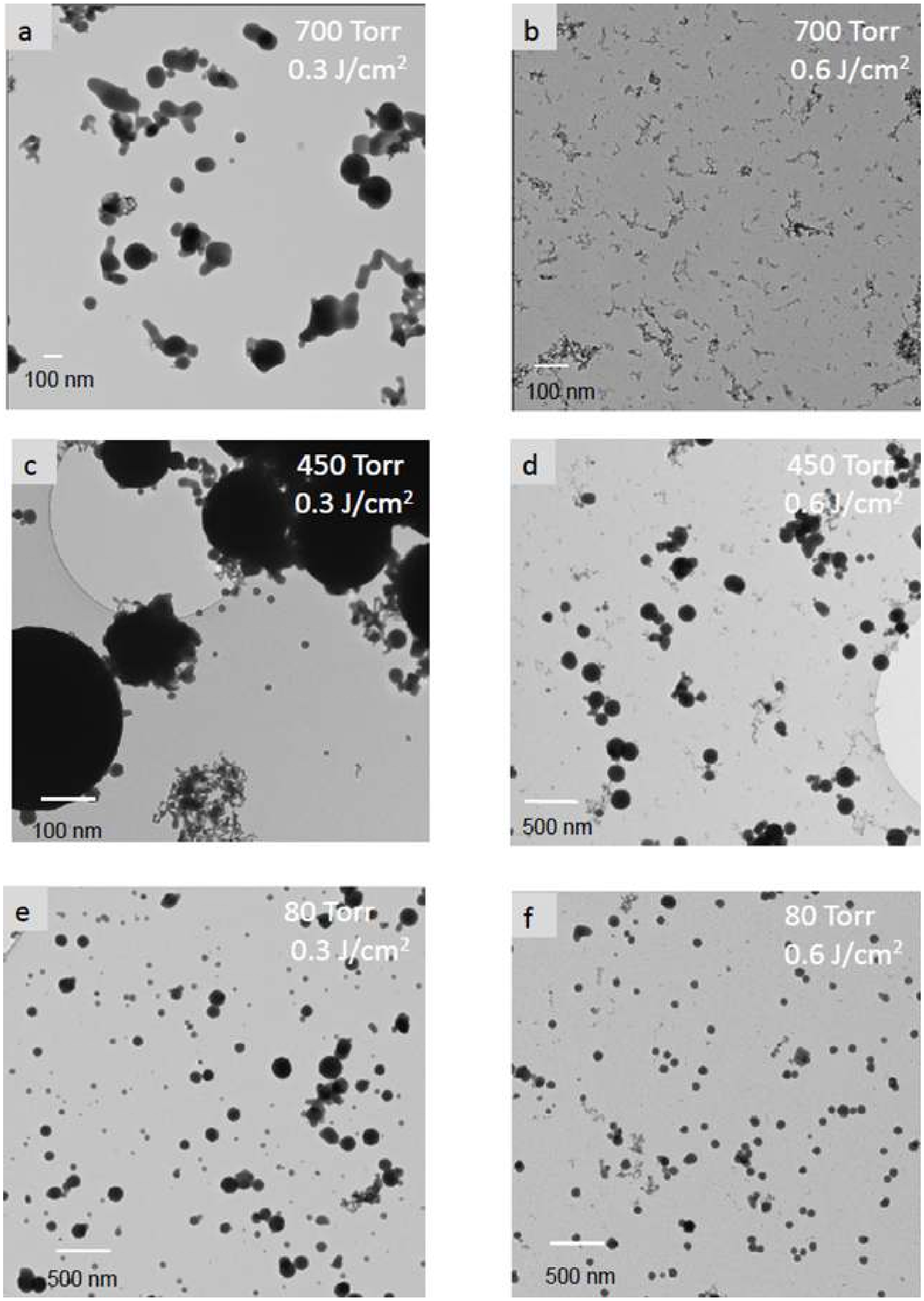

Fig. 16 – Transmission electron microscopy images showing effects of laser energy density and total pressure on nanoparticle shape and morphology.

4.5 Effect of Total Pressure

The overall effect of total pressure on the CaP nanoparticle morphology is quite apparent in Fig. 16. As the pressure increases, it is clear that the large spherical-like nanoparticles (100-300 nm) exhibit more signs of aggregation. For the sample deposited at 80 Torr (lowest pressure in the series), the large spherical-like particles show almost no aggregation. Substantially more aggregation is seen at 450 Torr, and even more at 700 Torr. This observed trend toward increased aggregation at higher pressures can be understood in terms of the time that particles spend in the aerosol phase between formation and deposition. Because particle transport is related to the volumetric flow rate, the actual transport velocity is inversely proportional to the pressure. Particles produced at 80 Torr, 450 Torr, and 700 Torr, take 0.7 s, 4.4 s, and 6.8 s, respectively to traverse the aerosol reactor. Consequently, the higher the pressure the longer the time for particles to interact and form aggregates. Increasing degree of aggregation with rising pressure is also seen in the smaller nanoparticle aggregates from the vapor phase. While they are clearly below 100 nm at 80 Torr, their vast majority have passed the 100 nm threshold at 700 Torr.

Although these irregularly shaped particles are not the archetype nanostructure that is often associated with biomedicine applications, it is worth mentioning that these irregular shapes at the nanoscale may represent significant patterns of bioactivity and further investigations on their biocompatibility is warranted.

4.5 Summary of Results

This short chapter has reviewed the basic characteristics of the nanoparticles produced by laser ablation of HA at room temperature and in an inert ambient. Two kinds of primary particles are normally formed: (i) dense and compact particles tending to spherical shape, most likely expelled from the targets as molten droplets (~100 nm); and (ii) small aggregates (20-100 nm) with primary particles < 10 nm, clearly of gas-phase origin. The compact, spherical-like particles are favored at low energy densities. At high energy density values these particles are still widespread but are now accompanied by the small aggregates of gas-phase origin. Both classes of particles are observed to undergo enhanced aggregation as the system pressure increases from 80 Torr to 700 Torr. This aggregation leads to samples dominated by fractal-like aggregates. XRD studies on samples produced at room temperature in inert ambient showed no evidence of long-range ordering in these particles, revealing the essentially amorphous nature of the nanoparticles. In addition to their complex shapes that might have unexplored bioactivity potential, their amorphous nature might also exhibit fast dissolution, consistent with rapid ionic release and resorbability needed in applications such as drug delivery and bone repair.

CHAPTER 5

AGGREGATION-FREE SIZE-CONTROLLED HYDROXYAPATITE NANOPARTICLES

5.1 Introduction

HA is perhaps the most widely studied of all CaP material. In terms of applications, preparations containing this compound in bulk or microcrystalline form have been used for decades in orthopedics and dentistry [128, 129]. Exploring how the outstanding biocompatibility of HA can be expanded even further in nanophase configurations, is an exciting frontier in bioceramics research [41]. In this regard, synthesis techniques able to control the characteristics of nanophase HA-based materials are essential for research progress. In this chapter we show how gas-phase laser synthesis can be applied specifically to the synthesis of HA nanoparticles with interesting advantages. The temperature control of gas-phase processes, the synthesis in OH-rich environments, and the possibility of mobility classification described earlier in this dissertation are particularly well suited for controlling the characteristics of HA nanoparticle ensembles. Synthesized particles first analyzed by TEM and AFM for determination of their morphology and degree to which their size can be controlled. AFM also allows quantification of the areal density of nanoparticles deposited on surfaces to create HA-based substrates with controlled nanoscale topography. XRD is then used to ascertain the crystal structure of similar particles. Surfaces of controlled nanotopography are subsequently investigated with respect to the ability of RGD peptides to adsorb on them. Finally, a brief exploration is carried out of the use OA to characterize the same particles in solution.

5.2 Synthesis Configuration

The experimental configuration already described in Chapter 3 (Fig. 10) was used for HA nanoparticle with temperatures in the ablation chamber adjusted in the 700-900^{o}C range. A continuous flow of an Ar/H_2O mixture was sustained through the ablation chamber at a total constant pressure of 960 mbar, monitored through the capacitance pressure gauge. Energy densities of 3-5 J/cm^2 and repetition rates of 1-10 Hz were used to ablate the HA target. The most important parameters that control HA crystallization are the ablation chamber temperature and the partial pressure of water vapor. These parameters were therefore varied within the dynamic range of the system, to determine their effect on HA nanoparticle formation.

5.3 Nanoparticle Morphology and Size Control

Fig. 17(a) shows a TEM image of nanoparticles produced with laser energy density of 5 J/cm^2 in a partial pressure of water p_{H_2O}=160 mbar at a temperature of 800°C and deposited on a holey carbon TEM grid. The voltage on the DMA was set at –324 V. Approximately 200 particles are visible in the image. A survey of the entire grid revealed the same general appearance with well separated particles and no evidence of widespread aggregation. As shown in the close-ups of Fig. 17(b), these particles are compact with a tendency to spherical shape. With rare exceptions, the morphology of individual particles is consistent with particle formation from the vapor phase by nucleation followed by coagulation growth. Because coagulation takes place in the hot zone of the ablation chamber, coagulated particles coalesce into the compact particles observed. The inset of Fig. 17(a) shows the size distribution obtained from the image. Data points correspond to a histogram of diameters while the solid lines represent log-normal distributions fitted to the data. The data is well represented by two log-normal distributions with geometric mean diameters $\overline{D}_{pg}$ = 39 nm and $\overline{D}_{pg}$ = 70 nm, both with geometric standard deviation $\sigma_g \approx 1.2$. The presence of two peaks is not surprising. As discussed earlier, this is expected in an aerosol that contains multiply charged particles in addition to singly charged ones. An interesting observation, however, is that for 39-nm and 70-nm particles to possess the same mobility, they must be singly and *triply* charged, respectively. This seems to indicate that the aerosol is dominated by particles carrying either a single elementary charge or three elementary charges.

Figs. 17(c) and (d) show size distributions for similarly produced nanoparticles deposited on Si substrates and analyzed by AFM. Samples shown in Figs. 17(c) and (d) were produced while applying voltages of –231 V and –430 V to the DMA, respectively. In these cases, the size distributions obtained correspond to histograms of particle heights determined by AFM. Good representations of the data again require size distributions with more than one peak. The data in Fig. 17(c) is well represented by two log-normal distributions with $\overline{D}_{pg}$ = 20 nm ($\sigma_g \approx 1.4$) and $\overline{D}_{pg}$ = 36 nm ($\sigma_g \approx 1.3$), while Fig. 17(d) shows peaks with $\overline{D}_{pg}$ = 39 nm ($\sigma_g \approx 1.4$) and $\overline{D}_{pg}$ = 70 nm ($\sigma_g \approx 1.3$). These peak positions are again consistent with each sample being produced by an aerosol dominated by singly and triply charged particles. It is significant that the use of an aerosol neutralizer between the ablation chamber and the DMA led to samples well described by a single log-normal distribution, confirming that the observed secondary peaks are indeed due to multiply charged particles. A neutralizer was not widely used in our experiments because it substantially decreases particle throughput due to losses to its inner walls. Since samples analyzed by TEM and AFM were produced using the same mobility classification parameters, all samples must have fundamentally the same size distribution width. The fact that size distributions obtained by AFM appear broader ($\sigma_g \approx 1.3$-1.4) than those measured by TEM ($\sigma_g \approx 1.2$) is most likely due to a systematic broadening of height data through the AFM measurement. The widths obtained by direct electron imaging (TEM) are probably most representative of the actual width of the size distributions.

For comparison, Fig. 17(e) shows a TEM image of typical nanoparticles produced without mobility classification. An assortment of particles with a very broad variety of shapes and sizes, ranging from 50 nm to 900 nm, is observed. Isolated nanoparticles 50-100 nm in size are seen alongside large aggregates in the 200-900 nm size range. The inset of Fig. 17(e) shows the size distribution obtained from the same image. A log-normal fit to the histogram of projected-area diameters yields $\overline{D}_{pg} = 62$ nm with $\sigma_g \approx 2.5$, indicating a highly polydisperse original aerosol population. Particularly noteworthy is the tail of the large-size end of the distribution, which comprises a significant number submicron particle aggregates (0.5-0.9 μm). These very large aggregates, which are generally undesirable in biomedical applications [41], are a result of particle coagulation in areas sufficiently cold to prevent coalescence.

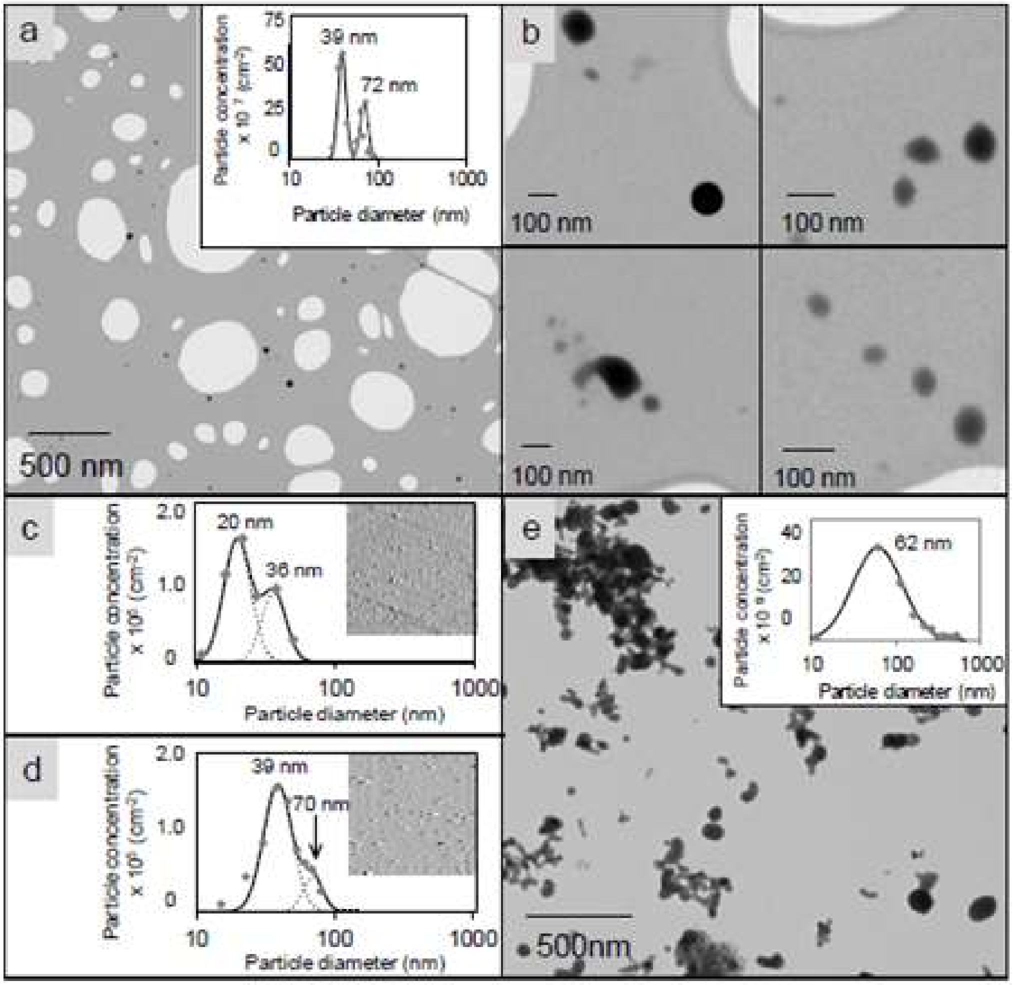

Fig.17 – (a) TEM image of nanoparticles synthesized with laser energy density of 5 J/cm^2, p_{H_2O}=160 mbar, and T = 800°C with DMA set at a voltage of –324 V. Inset shocws particle size distribution from image. Solid line fitted to the data points represents two log-normal distributions. (b) Close-ups of select nanoparticles. Size distributions of samples deposited with DMA voltage of (c) –231 V and (d) –430 V. In parts (c) and (d), the solid lines fitted to the data points represent superposition of two log-normal distributions (dotted lines). (e) TEM image of polydisperse nanoparticles and conrresponding size distribution (log-normal fit).

5.4 Nanoparticle-based Substrates with Controlled Nanotopography

Fig. 18 shows AFM scans of nanoparticles deposited on Si substrates for different amounts of time. Since gas-phase particle concentrations are sufficiently low ($< 10^5 \text{cm}^{-3}$), nanoparticles are deposited on the substrate without substantial pile-up. Hence, as the particle number density increases, the inter-particle spacing decreases. Although the nanoparticles are randomly distributed on the surface, they have well-defined average particle height and separation, specifying a reasonably well-controlled nanotopography. Such substrates may be useful in studies of the effects of nanotopography on the behavior of living cells that interact with HA.

5.5 Effect of Temperature and Partial Pressure of Water on Nanoparticle Crystal Structure

Ascertaining the chemical and crystal phase characteristics of the deposited nanoparticles is of critical importance for predicting their bioactivity. We have used XRD for this purpose. Fig. 19(a) shows a standard XRD pattern of HA corresponding to a hexagonal structure ($P6_3/m$ space group) with lattice parameters a = 9.4240 Å and c = 6.879 Å. Fig. 19(b) displays XRD patterns obtained from samples of polydisperse particles produced in this work with a laser energy density of 5 J/cm^2, p_{H_2O} =160 mbar, and various temperatures in the range T = 750-800°C. The clear presence of many reflections of HA in Fig. 19(b), essentially matching the standard, demonstrates the formation of crystalline HA nanoparticles. A temperature of 800°C seems to be particularly conducive to the production of crystalline HA with well defined (211), (112), and (300) reflections. In the 850-900°C temperature range, evidence of the formation of a distinct unidentified phase is noted as indicated by the presence of a reflection slightly below $2\theta \approx 31°$, and marked by a cross ($^{+}$). Although very weak, this unidentified peak is evidence that higher temperatures may lead to the formation of crystalline phases other than HA in the samples. This is a topic that is revisited in greater detail in Chapter 6.

Fig. 19(c) shows the effect of varying the partial pressure of water (and thereby the OH^{-} availability) for a temperature of 800°C in the ablation chamber. Although some evidence of HA formation is seen for p_{H_2O} = 30-120 mbar, with development of weak (211), (112), (300) and (202) reflections, these peaks only become clearly distinct for synthesis at 160 mbar. Not surprisingly, the samples with weak HA reflections also exhibit a calcium oxide (CaO) peak at $2\theta \approx 37.5°$, indicated by an asterisk (*) in Fig. 4(c). Formation of CaO during laser irradiation of HA is well documented and expected under the dehydroxylating conditions of low partial pressure of water [15]. As the water content in the ambient is increased, the CaO reflection appears to diminish in intensity completely disappearing for p_{H_2O}=160 mbar.

5.6 Peptide Adsorption on HA Nanoparticle-based Substrates

As discussed in Section 2.4, the HA nanoparticle-based substrates developed in this dissertation may provide useful surfaces for studies involving cell attachment via peptide ligands. In order to assess their potential in this regards, polydisperse HA nanoparticle substrates were synthesized using the gas-phase laser process with the apparatus shown in Fig. 10 and subjected to peptide studies. Two sets of samples were prepared on atomically flat, microelectronics-grade Si substrates. Samples with low number density of HA nanoparticles (deposition time ~ 2.5 min) as well as samples with high number

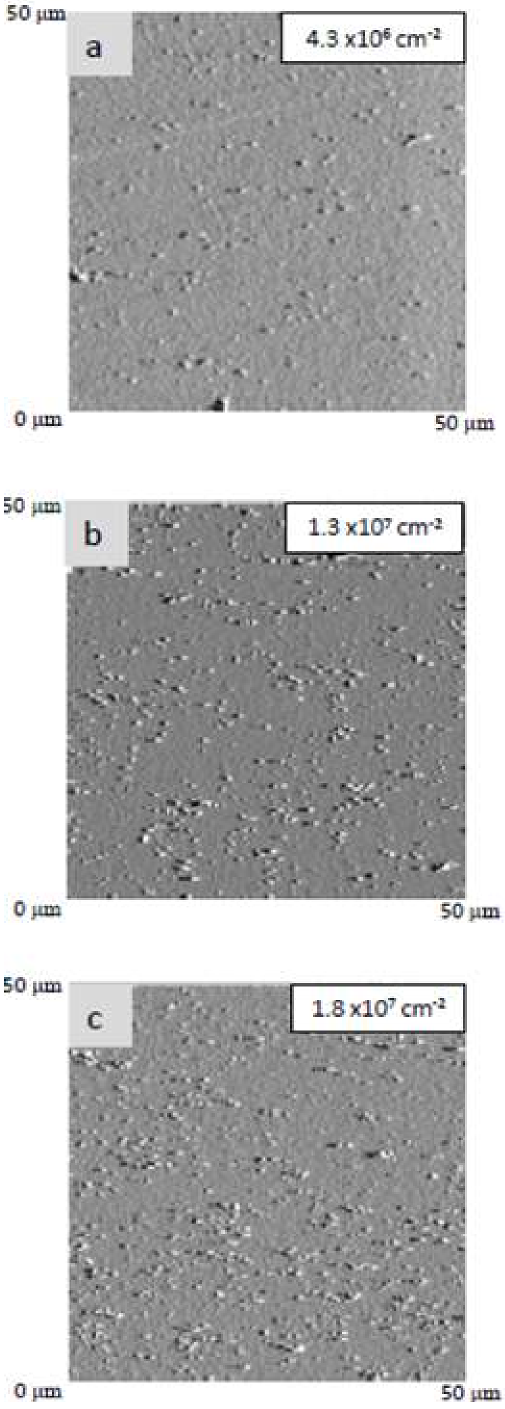

Fig.18 – AFM scans of samples produced with laser energy density of 5 J/cm^2, p_{H_2O} =160 mbar, and T = 800°C with DMA at a voltage of –324 V. Samples deposited for (a) 5 min., (b) 30 min., and (c) 90 min.

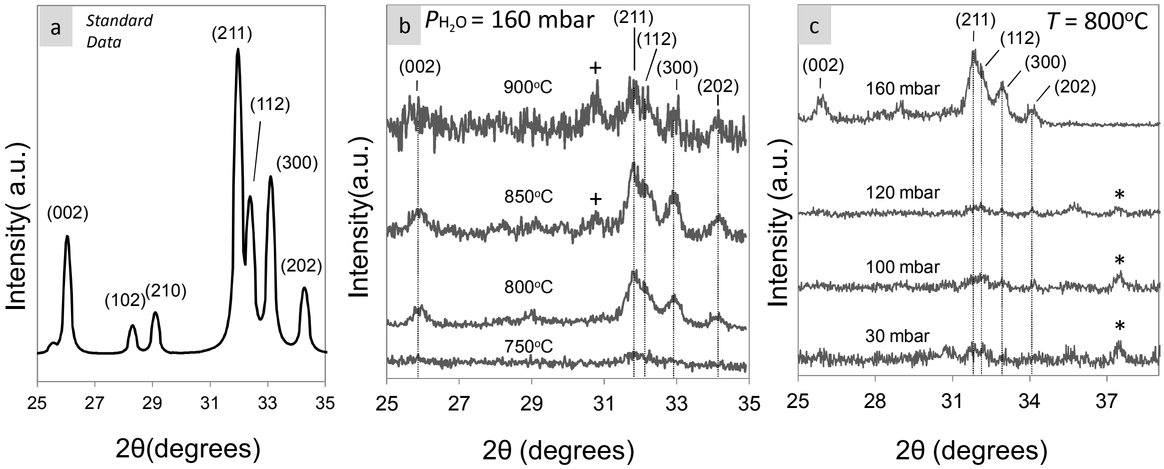

Fig. 19 – (a) Standard XRD pattern of pure HA. (b) XRD patterns of polydisperse nanoparticles produced at various temperatures (5 J/cm^2; p_{H_2O}=160 mbar). Indexed peaks correspond to HA. Peak marked by (+) is not a reflection from HA and remains unidentified. (c) XRD scans of polydisperse nanoparticles produced at various partial pressures of water (5 J/cm^2; 800^o C). Reflection marked by (*) is ascribed to CaO.

density (deposition time ~ 5 min) were produced. A third set of plain Si substrates (with no HA nanoparticles) was used as a control sample.

The peptide GPenGRGDSPCA (948.1 g/mol), which has reported selectivity for the VN receptor [83], was the starting peptide for the experiment. A modification of this peptide sequence was synthesized by American Peptide Co., Inc. (Sunnyvale, CA) to create the sequence EEEEEEEGPenGRGDSPCA–FITC (2369.4 g/mol; E_7RGD–FITC for short). The lyophilized peptides were reconstituted in deionized water and diluted in Tris–buffered saline (TBS) to final peptide concentration. Each set of sample was placed in the bottom of low attachment cell culture dishes and coated with 10μM concentration of E_7RGD–FITC and then incubated for 2.5 hrs at 35°F. The fluoroscein conjugate (FITC) allows direct visualization of the immobilized peptide using fluorescence microscopy. Each substrate was mounted on a microscope slide and was visualized using fluorescent Nikon SMZ-U stereomicroscope at a 40X magnification.

Fig. 20 (a) shows a TEM image of the particle morphologies typically seen in the polydisperse samples used here for peptide adsorption. As discussed previously, a very broad variety of shapes and sizes ranging from 20 nm to 900 nm is seen. The inset of Fig. 20(a) shows the corresponding size distribution. Figs. 20(b) through (d) show the effectiveness of these kinds of substrate in promoting peptide adsorption. For the purpose of establishing a reliable baseline, Fig. 20(b) shows the fluorescence microscopy image obtained after the E_7RGD–FITC suspension was immobilized on a plain Si substrate with no HA nanoparticles (control sample). Since no fluorescence is visible on the control sample, we surmise that no peptide adsorption takes place. The inset of Fig. 20(b) shows an 8-bit grayscale intensity histogram for the image. The delta function-like peak is

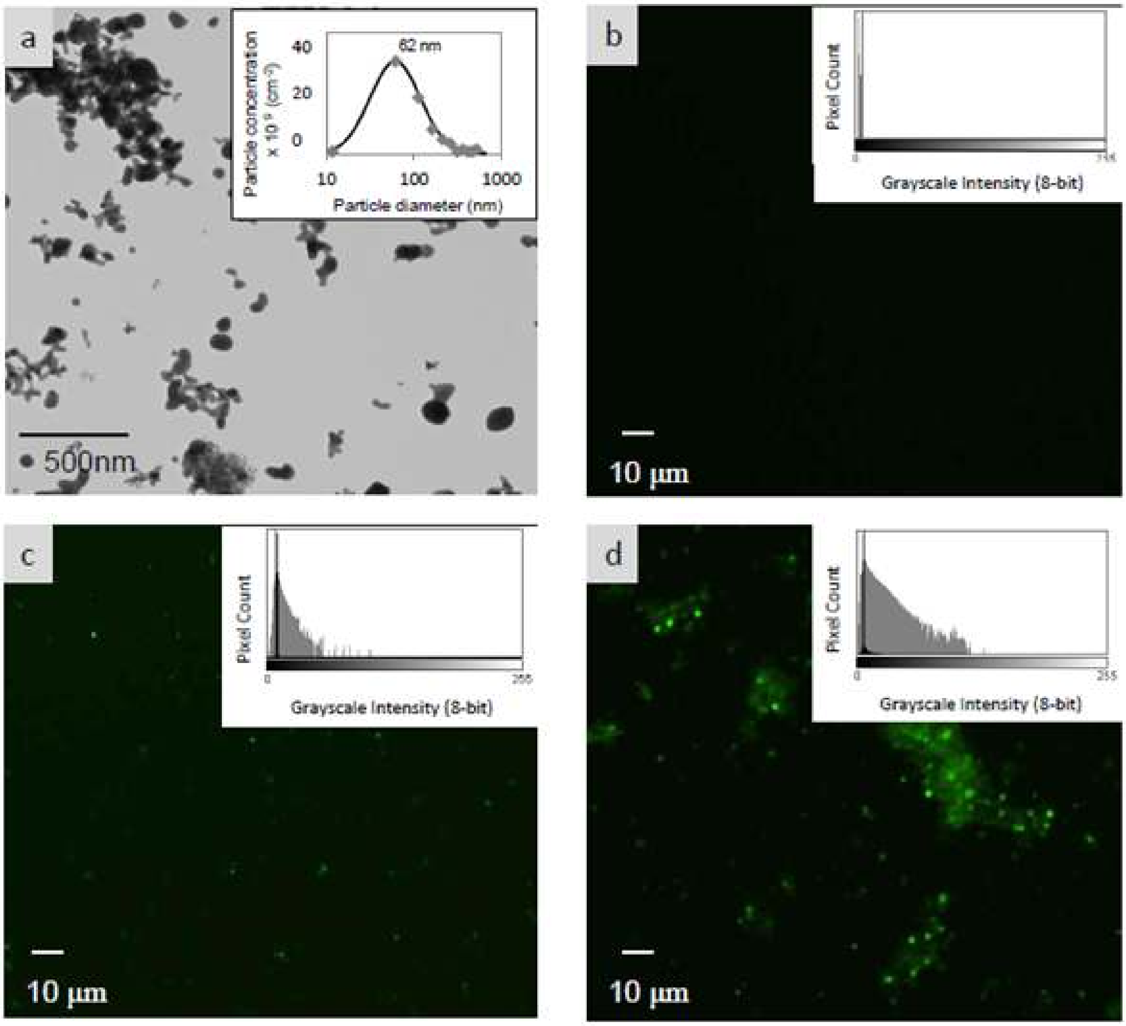

Fig.20 – (a) Typical polydisperse nanoparticles produced by laser/aerosol system. Inset shows the size-distribution from the image. (b) through (d) show selective attachment of E_7RGD–FITC peptide on the nanoparticle substrates. Insets of (b), (c) and (d) show the 8-bit grayscale intensity histogram for the images.

obtained because essentially all pixels have the same low intensity. The Si substrates therefore seem to be ideal surfaces for conducting these studies as they do not, of themselves, promote any peptide adsorption to their surfaces. Figs 20 (c) and (d) show fluorescence microscopy from E_7RGD–FITC peptides immobilized on the low- and high-density HA nanoparticle samples, respectively. It is immediately evident that the binding of E_7RGD–FITC peptide scales with the number density of HA nanoparticles on the surface. The broadening of the intensity histograms for both cases is a consequence of the greater fluorescence of the samples in panels (c) and (d). It is evident that the number of pixels with high fluorescence intensity is found in the sample with the highest concentration of HA nanoparticles [Fig. 20(d)]. The HA sample with high number concentration also shows significant evidence of peptide aggregation, as regions of intense fluorescence (bright spots) are noted on the sample. Since the actual peptide molecule cannot be resolved with the resolution of fluorescence microscopy, these bright spots are interpreted as large clusters of many peptides. It is also evident that the number of clusters also scales with the number density of HA nanoparticles. It is also worth mentioning that, overall, the spatial pattern seen in the fluorescence microscopy image agrees with the expected spatial distribution of HA nanoparticles in these polydisperse samples. It is apparent that these HA nanoparticle-based substrates offer excellent adsorption surfaces for E_7-containing peptides.

Size-controlled HA nanoparticle substrates synthesized using the apparatus of Fig. 10 were also exposed to E_7RGD–FITC peptides according the protocol used for polydisperse samples. These size-controlled HA nanoparticles were deposited on triangular Si wafers in the nozzle-to-plate electrostatic precipitator by applying a voltage of –231 V between the DMA electrodes, corresponding to particles in the 20-40 nm size range according to the results of Section 5.3. A voltage of –400 V was maintained on the substrate with respect to the deposition nozzle to maximize particle collection. Three sets of samples were produced with number concentration of HA particles estimated as 0.4 x 10^7 cm^{-2}, 1.3 x 10^7 cm^{-2}, and 1.8 x 10^7 cm^{-2} were deposited by using deposition times to 5 min, 30 min, and 90 min, respectively, with an gas-phase aerosol number concentration in the 2-6 × 10^5 cm^{-3}. Fig. 21(a) shows images obtained by fluorescence microscopy. Careful inspection of the images under suitable illumination reveals, even to the naked eye, a small brightening of the images with increasing nanoparticle concentration. The images were acquired simultaneously under the same focusing conditions and acquisition parameters. This provides some confidence that the small change observed is significant. A quantitative analysis of the intensity of the images is shown in Fig. 21(b). 8-bit grayscale intensity histograms of the images are shown with evidence of a small but discernible shift of the mean image intensity to higher values with increasing nanoparticle concentration. The intensity histograms are also observed to broaden as the concentration of particles increases, with substantial pixel counts in the high-intensity tail of the histograms.

As observed in the polydisperse samples exposed to peptides, higher concentrations lead to peptide clustering. Consequently, increased cluster count also seems to be indicative of higher nanoparticle densities on the substrate. Fig. 21(c) shows how the number of discernible peptide clusters (bright spots on the fluorescence microscopy field) changes with HA nanoparticle number density for an equivalent set of samples. The inset

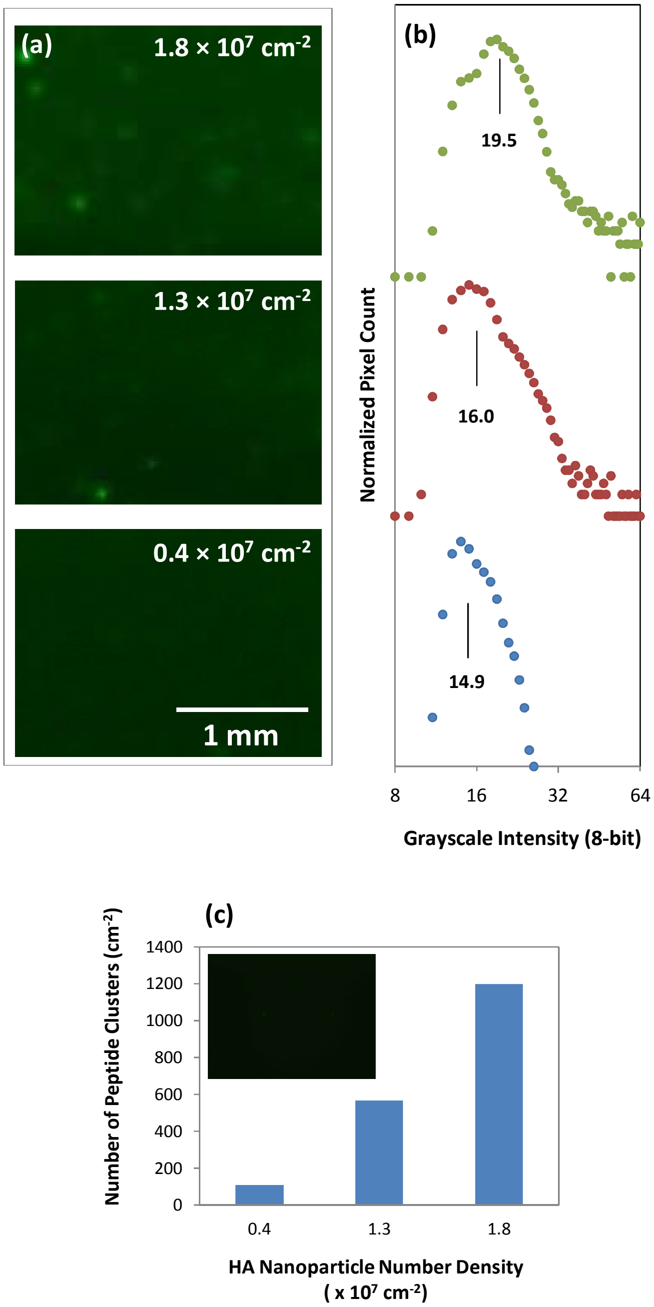

Fig.21 – (a) Fluorescent microscopy images showing peptide attachment on size-selected nanoparticle substrates with varying densities. (b) 8-bit grayscale intensity histograms of the images (c) Bar graph showing correlation between HA nanoparticle density and number of peptide clusters that are attached to the nanoparticle substrate.

in Fig. 21(c) shows an example of visible clusters counted for measuring the dependence seen in the figure. Overall, these results in peptide adsorption show that the HA-nanoparticle substrates synthesized from the gas-phase are promising for fine control of peptide adsorption. They might enable both, variation of monolayer peptide distributions on the surface and low degrees of peptide clustering permitting cell studies that could reveal subtle effects in cell adhesion phenomena.

5.7 Optical Absorption Measurements

Because many applications of HA nanoparticles involve their dispersion in liquid media, we have also explored the suspension of the gas-phase laser synthesized particles in a water-based solution. In order to assess the behavior of the particles in this new environment, we performed OA measurements on the dispersed size-selected HA nanoparticles. As explained in Chapter 3, dispersion was achieved by replacing the electrostatic precipitator in the apparatus of Fig. 10 by a bubbler. Laser-synthesized HA particles produced with a laser energy density of 5 J/cm^2 and p_{H_2O}=160 mbar were processed through the DMA using a voltage of –324 V) and suspended in deionized water.

Fig. 22 shows absorbance data for this HA nanoparticle suspension. These samples lend themselves well to optical studies. If properly interpreted, the interaction of light with nanoparticles in suspension can yield quantitative information about their concentration, morphology, and electronic states. For comparison, absorbance is also shown for a commercial HA micro-powder that was used as the starting material for making the ablation targets (97.5% purity, Plasma Biotal Ltd.). The observed spectra may be understood as a composite of the fundamental absorption of HA, the scattering of the light by

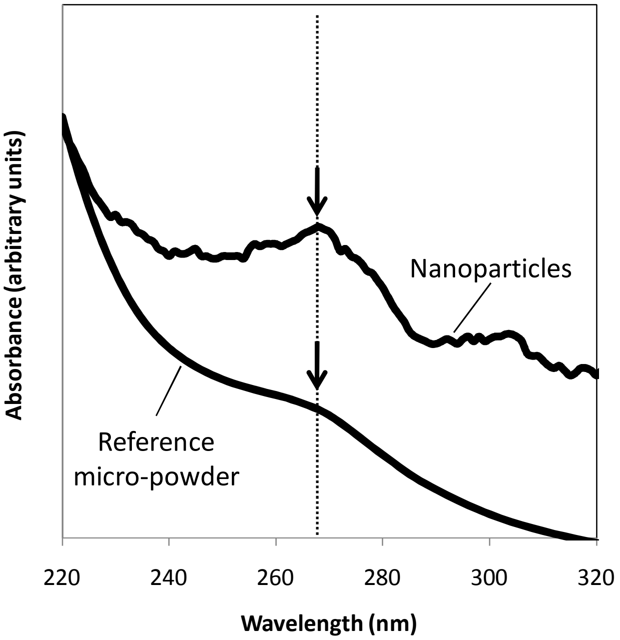

Fig. 22 – The absorption of calcium phosphates in differing forms is compared here. The arrows indicate a common area of “below band gap” absorption for commercially provided hydroxyapatite micro powder and laser ablated nanoparticles.

the sub-micron particles and one or more below band gap absorption features. Being an insulator with energy gap of 5eV, it is expected that a sharp absorption edge should be evident at ~250nm. As in many insulators, the absorption edge is known to follow the Urbach rule given by

$$\alpha(E) \propto e^{\sigma(E-E_g)/K_B T}, \tag{5}$$

where σ is a fitting parameter, E is photon energy, K_B is Boltzmann's constant, and T is temperature [130]. This absorption edge should be superimposed on a scattering background strongly dependent on the particle size. Also, defects or impurities in the material could lead to absorption feature below the band gap energy.

Fig. 23(a) shows the measured absorbance for an HA nanoparticle sample with a nominal nanoparticle concentration of 2×10^8 cm^{-3} . The sharp short wavelength ascent of the absorbance and the general trend of the data can be matched by superimposing the Mie scattering of 60 nm spherical particles (shown as "Scattering Absorbance" in the figure.) and an Urbach tail with E_g = 4.5 eV (shown as "Urbach Absorbance"). When the scattering and the Urbach tail are subtracted from the measured spectrum, the data yields the "below-band-gap" absorption of the material as shown in Fig. 23(b). The HA nanoparticle suspension thus show two very well defined absorption peaks that are likely to be related to specific electronic states in the particles themselves. One peak is centered around 270 nm whereas another peak of lower intensity is found at ~300 nm. Changes in the intensity of these "below band gap" absorption features could allow quantification of nanoparticle concentrations. If reproduced other more resorbable CaP phases, tracking of

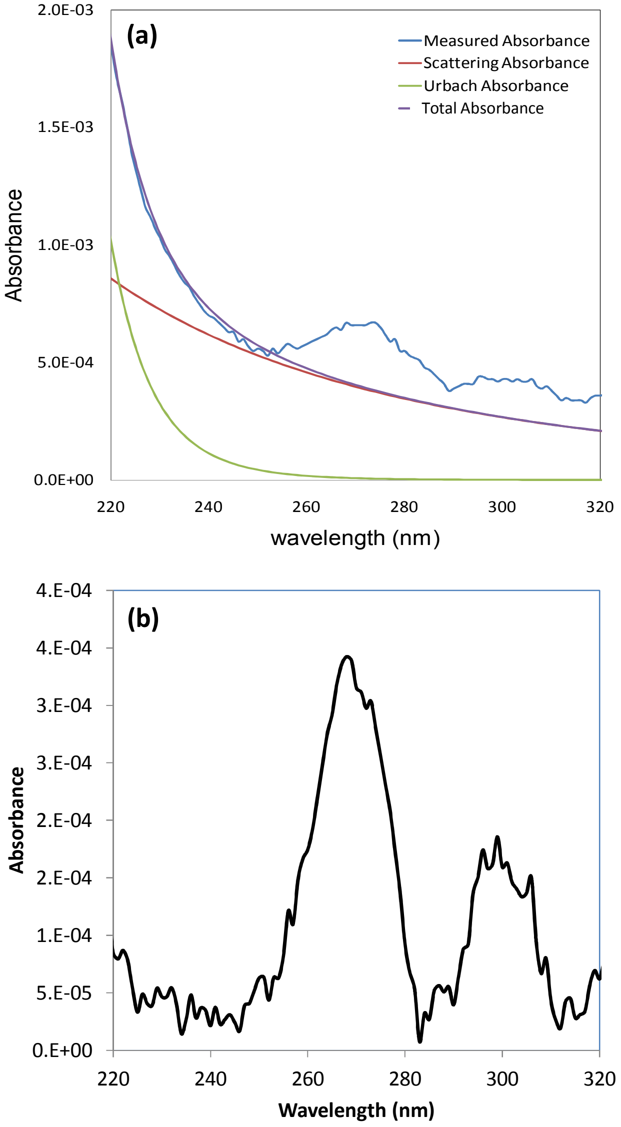

Fig. 23 – (a) Typical measured raw absorbance data, Mie scattering absorbance corresponding to 60 nm HA nanoparticles and Urbach tail for 4.5 eV band gap. (b) Below band gap absorbance for 60-nm HA nanoparticles suspended in water with the subtraction of Mie scattering and an Urbach tail for energy gap of 4.5 eV.

the time evolution of these intensities might also allow assessment of the stability of CaP nanoparticles in solution.

These basic measurements show that although the focus of this dissertation is on gas-phase synthesis of nanoparticles for deposition on surfaces, the fabrication approach developed is compatible with use of these particles in solution, which of course expands significantly the range of applications of gas-phase synthesized bioceramic particles.

5.8 Summary of Results

This chapter has demonstrated the synthesis of aggregation-free, size-controlled HA nanoparticles using the described combination of laser-induced gas-phase generation and aerosol processing. Particles were produced in a high-temperature environment with controlled partial pressure of water by laser ablation of an HA target. Laser-generated particles underwent mobility classification and were deposited with narrow size distributions on solid substrates in adjustable number concentrations, without appreciable aggregation upon deposition. TEM and AFM measurements established the ability to deposit nanoparticles with reasonably well controlled size below 100 nm and size distributions substantially narrower than in cases without mobility classification. At a laser fluence of 5 J/cm^2, a temperature of 800°C and partial pressure of water of 160 mbar were found to be the most suitable conditions for HA nanoparticle formation. Successful adsorption of E_7RGD-FITC peptides on polydisperse as well as size-controlled HA nanoparticle substrates demonstrate that these substrates may enable studies for decoupling the effects of nanotopography and biochemical cues in integrin-mediated cell adhesion. The gas-phase synthesize particles can also be suspended in liquid media, as confirmed by OA experiments, indicating their applicability in many other biomaterials approaches that require particles in solution.

CHAPTER 6

NANOPARTICLE-BASED BIPHASIC CALCIUM PHOSPHATE SUBSTRATES

6.1. Introduction

Research in CaP bioceramics over the past decade has devoted substantial attention to biphasic materials composed of nonresorbable HA and a resorbable phase such as tricalcium phosphate (TCP) [14, 24] or tetracalcium phosphate (TTCP) [15]. The partial dissolution of the bioresorbable phase in biphasic CaPs is considered beneficial because it may stimulate cellular activity leading to more bone apatite formation at the interface between the CaP material and the actual bone tissue [41-43]. Extensive research has been carried out in biphasic CaP materials in bulk form and as coatings. In those contexts, if the dissolution of the bioresorbable phase is too rapid, it can deteriorate the mechanical integrity of the system. Hence, it is very important to find the optimum amount of the highly resorbable phases in the biphasic calcium phosphates so that they can enhance bioactivity in scaffolds, coatings, and bulk configurations, which should improve the biological performance of these systems in the long term, while avoiding their mechanical failure in the short term.

The ability to fabricate CaP nanoparticles that would also exhibit a biphasic configuration, would be an exciting outcome for biomaterials research. One can conceive of such particles as a composite system whose resorbable portion could provide ionic stimuli for the biological environment, while its non-resorbable fraction could serve as nucleation sites for biomineralization, anchoring points for specific biomolecules, and imparters of improved stiffness to the overall system. A broad range of applications suggest themselves in drug delivery as well as in bone tissue engineering and bone repair.

The ideal phase make-up of such biphasic particles as well as their nano- and microstructure evidently represent open questions since very little research has been conducted in this area. In the case of bulk systems, the HA/TCP combination has been widely studied because it can be prepared by simple methods involving the sintering of calcium-deficient apatites at or above 700ºC [39, 40]. Biphasic samples of HA and TCP prepared by these methods have been the object of frequent investigations also because of its anticipated compatibility with large-scale production of bone substitute systems such as scaffolds and grafts. Although this concept has been applied mainly to the HA/TCP combination because of the convenient, well-established methods of materials preparation, it can evidently be extended to biphasic system composed of nonresorbable HA and other bioresorbable phases. There are also reports in the literature of studies in biphasic HA/TTCP in the form of thin coatings [15]. Both of these combinations (HA/TCP and HA/TTCP) have proven thermodynamically stable and exhibited gains in bioactivity as bulk or coatings. Evidently, it is not known whether these combinations offer the best phase association in the case of nanoparticles. The larger surface area of nanophase systems and the modified kinetics of dissolution may lead to quite different behavior in the nanoscale. Despite these unknowns, the research in this dissertation was carried out with the awareness that the "far from equilibrium" conditions that characterize laser synthesis could lead to the formation of CaP particles with more than one crystallographic phase. It has in fact been shown that laser synthesis is particularly effecting in the generation of biphasic HA/TTCP coatings under dehydroxylating conditions [15]. We therefore anticipated that a similar phenomenon was possible in the context of gas-phase nanoparticle generation.

Initial evidence that another crystalline phase might develop in the laser synthesized nanoparticles was observed in the course of the experiments aimed at synthesis of pure HA nanoparticles and reported here in Chapter 5. As seen in Fig. 19(b), the X-ray pattern of nanoparticle samples produced at 850°C and 900°C show a reflection at $2\theta \sim 31°$ that cannot be assigned to HA. Because of the relatively low signal-to-noise ratio in the patterns of Fig. 19, it was not possible to ascertain the nature of the secondary crystal phase corresponding to this reflection. In this chapter, however, we show how further XRD data obtained at the higher-brilliance LNLS synchrotron light source provides evidence that a secondary CaP phase is present in the samples produced at higher temperatures.

6.2 Post-deposition Processing and Crystal Phase Make-up Analysis

The data shown in Fig. 19 (Chapter 5) revealed that as-deposited particles produced at temperatures in the 850-900°C range at p_{H_2O}=160 mbar might present a secondary crystalline phase, although the candidate reflections were very weak and broad [indicated by ($^+$) in Fig. 19]. In an attempt to enhance these reflections and facilitate XRD analysis, the samples whose patterns are shown in Fig 19 underwent post-deposition annealing at 800°C in Ar/H_2O ambient for 1 hr. The flow rate of Ar/H_2O mixture during annealing was maintained at 1 SLM. Post deposition annealing in Ar/H_2O ambient offers evidently the possibility of improving the crystal quality of the samples. Fig. 24 shows the effect of this treatment on the samples. The figure shows that annealing leads to

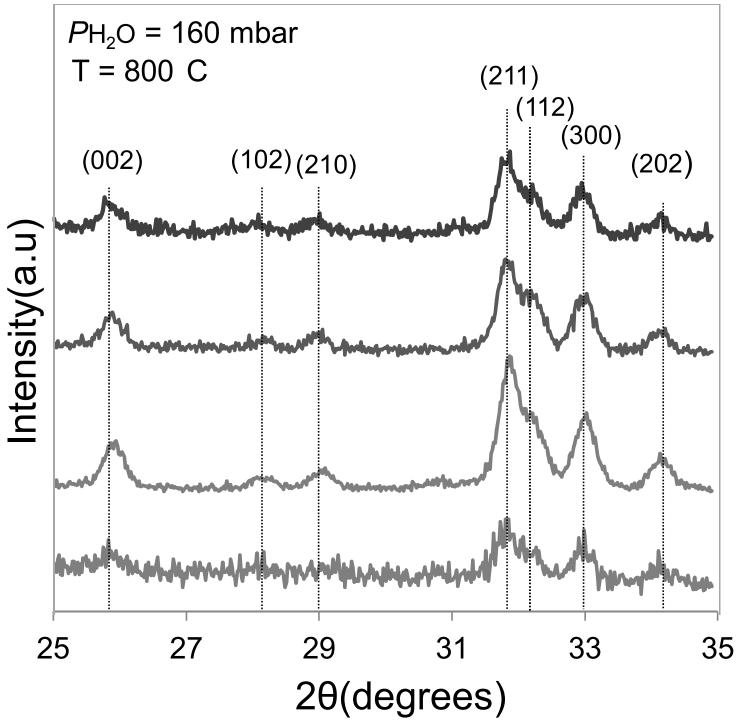

Fig 24 – X-ray diffraction patterns of polydisperse HA nanoparticles with post-deposition annealing at 800^{o} C for 1 hour (Indexed peaks correspond to HA).

sharper XRD reflections, overall. It is interesting to note that even samples that were essentially amorphous (750°C) or marginally crystalline (900°C) show substantial improvement in crystallinity with well-defined main reflections of HA. Some transformation also seems to take place in the unidentified reflection at $2\theta \sim 31°$. A careful inspection of the patterns shows that this reflection becomes more pronounced even for the sample produced at 800°C. XRD patterns obtained at the higher-brilliance source at LNLS bring significant clarification to the data as shown in Fig. 25. Fig. 26(a) actually shows the pattern obtained for the sample produced at 800°C. In addition to the very distinct reflections of HA, all well indexed to the hexagonal lattice with a = 9.424 Å and c = 6.879 Å ($P6_3/m$ space group), several low-intensity reflections that cannot be indexed to the HA structure are also observed in the pattern between ~29.5° and ~31.5° [indicated by vertical arrows in Fig. 26(a)]. Fig. 26(b) expands the 2θ range of these reflections. The non-HA reflections show substantial changes with variations in synthesis temperature. Four peaks in this range can be ascribed to the presence of tetracalcium phosphate, $Ca_4(PO_4)_2O$ (TTCP) in the samples. TTCP, which has the monoclinic structure as described in Chapter 2 (a = 7.018 Å, b = 11.980 Å, c = 9.469 Å, b = 90.88°) is one of the dehydrated calcium phosphate compounds. While the reflection assigned to the (221) peak of TTCP seems to remain unaltered for all temperatures, the peaks ascribed to the (040) and $(\bar{2}21)$ families of planes appear to shift in opposite directions and then subside as the temperature is raised from 750°C to 900°C. This effect is consistent with the existence of TTCP in the samples with a unit cell compressed along the c axis of the monoclinic structure. Table II shows the distortions in unit cell of the TTCP structure required to match the peak positions observed in Fig. 26(b).

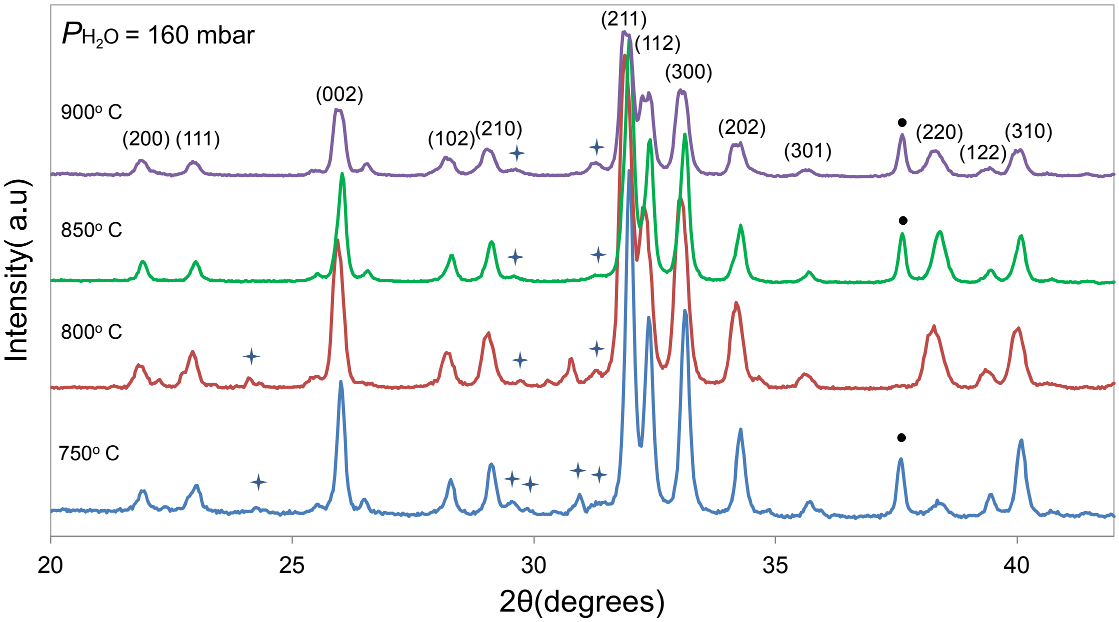

Fig. 25 – X-ray diffraction patterns of polydisperse HA nanoparticles (post-deposition annealing at 800° C for 1 hour) obtained using high brilliance synchrotron X- ray source. Indexed peaks correspond to HA and • corresponds to CaO.

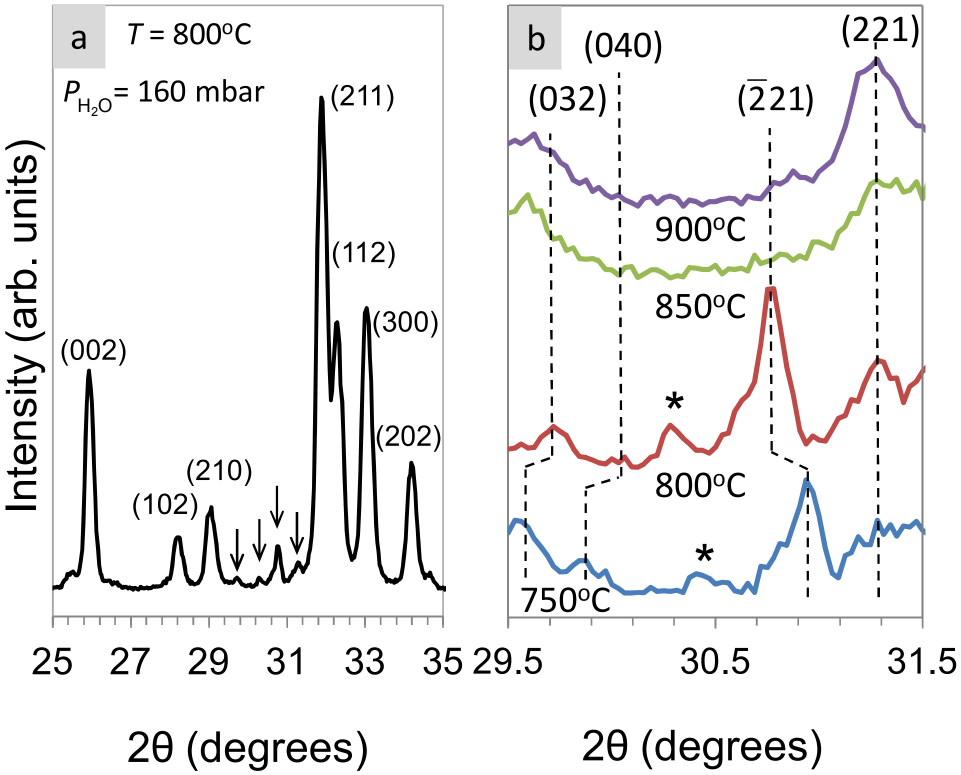

Fig. 26 (a) GIXD pattern of polydisperse particle-based substrate showing all reflections of HA; (b) Effect of temperature on GIXD reflections ascribed to TTCP.

Table II – Distortions in unit cell parameters of TTCP structure as a function of effect of synthesis temperature.

Pure HA	**Pure TTCP**	**TTCP 750^{o}C**	**TTCP 800^{o}C**	**TTCP 850^{o}C**	**TTCP 900^{o}C**
a = 9.424 Å	7.0230 Å	7.038 ± 0.007 Å	7.10 ± 0.04 Å	7.0230 Å	7.0230 Å
b = 9.424 Å	11.9860 Å	11.9860 Å	11.9860 Å	11.9860 Å	11.9860 Å
c = 6.879 Å	9.4730 Å	9.42 ± 0.02 Å	9.35 ± 0.02 Å	9.42 ± 0.02 Å	9.42 ± 0.02 Å
	β = 90.9^o	90.9^o	91.5^o ± 0.3	90.9^o	90.9^o

For both temperatures in which the (040) and $(\bar{2}21)$ reflections are reasonably recognizable (750°C and 800°C), the unit cell is likely to be compressed along the *c* axis and expanded along *a* axis. The most pronounced effect appears to be in the sample originally synthesized at 800°C, in which variations are seen in all four unit cell parameters, with an adjustment also needed in the angle β. Data for 850°C and 900°C suggest less distortions, although the subsiding of the peaks ascribed to the (040) and $(\bar{2}21)$ reflections at lower temperatures makes any definite statements unwarranted. The peak marked by an asterisk (*) in Fig. 26 (b) cannot be ascribed to HA or TTCP.

The distortions observed in the TTCP lattice parameters, as compared to the relaxed structure, suggest that this phase exists in the samples in close association with HA. Despite their different space groups, the unit cell dimensions of these two CaP phases allow for a variety of metric fits between their structures. Moreover, the positions of calcium and phosphate groups in HA and TTCP imply good chemical fits and possible topotactic transformations between the two. It is conceivable, for example, that TTCP grows epitaxially on pre-existing HA crystallites under dehydroxylating conditions. These findings suggest that it may be possible to fabricate biphasic HA/TTCP nanoparticles, which could be of great interest in biomedicine, as they would combine the desirable mechanical stability of nonresorbable HA, with the enhanced bioactivity of the resorbable TTCP phase, a combination of properties that is difficult to achieve in a single-phase material.

It is worth noting that the HA peaks remain essentially unchanged for synthesis in the explored temperature range (750-900°C; with P_{H_2O} = 160 mbar). However, an interesting second-order effect appears to take place in the 900°C sample. Fig. 27 shows a comparison between samples deposited at 800°C and 900°C. Fig. 27 shows evidence of a

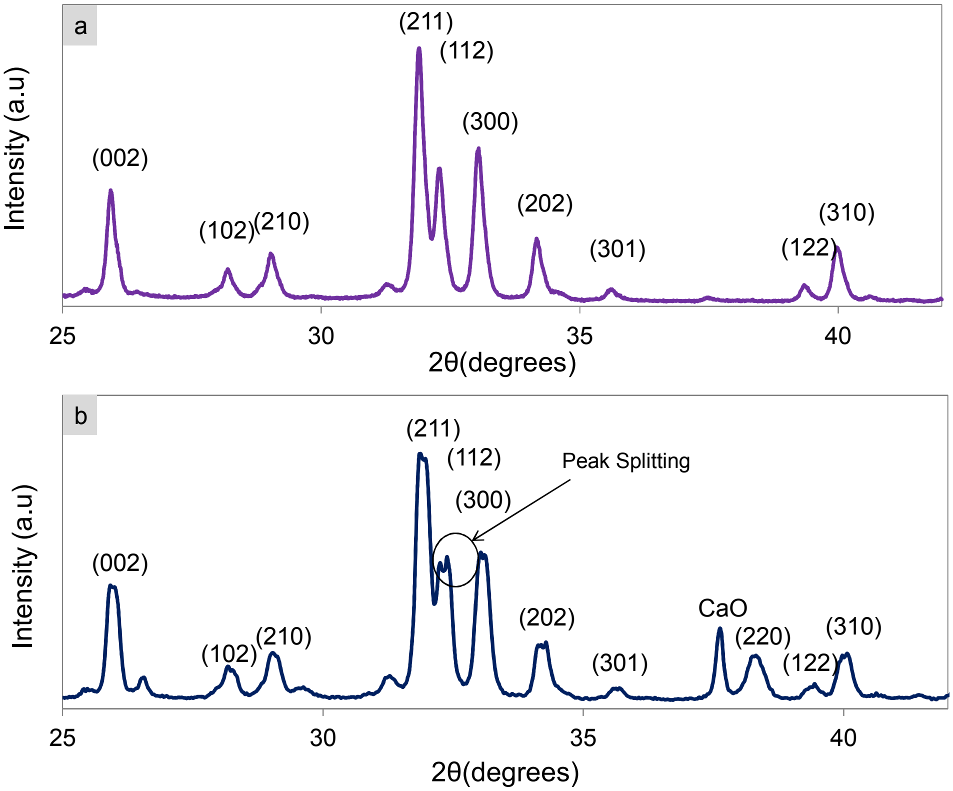

Fig. 27 – (a) and (b) XRD patterns of polydisperse HA nanoparticles synthesized at 800°C and 900°C temperature, respectively. HA peaks appear to split at temperature of 900°C.

“split” in all HA reflections while the HA reflections. Such peak splitting in XRD data normally occur when a single a material is present in a sample under two different stress conditions. This would lead to two HA structures with slightly distorted unit cells coexisting in the sample. One set of the peaks in the 900°C sample is essentially in the same angular positions as the peaks of the HA standard. The second set of peaks can be matched by a distorted HA structure with lattice parameters $a = 9.400$ Å and $c = 6.879$ Å, One noteworthy observation is presence of CaO in some of the samples. As seen in Fig. 25, samples in which CaO is present (750°C and 850°C) consistently show the stressed HA structure. Whereas the sample in which CaO is absent (800°C) seems to exhibit the relaxed HA pattern. The “double-peaked” sample (900°C) seems is well represented by a superposition of stressed and relaxed HA components. It is quite possible from these considerations, that the presence of the CaO phase, which is a cubic material, may be responsible for the HA component under stress.

It must be stated, of course, that post-deposition annealing is, in general, undesirable in polydisperse samples with elevated particle number concentration. In these kinds of samples many particles are in contact with each other. Annealing in this case can easily lead to coarsening and grain growth, which have negative impact in the biocompatibility of the material. Nevertheless, the result shown here, indicate that post-deposition annealing can help enhance some basic features in the XRD patterns of samples, facilitating the gathering of information about the system. It is also noted that if gains could be made in the residence time of nanoparticles in the hot zone of the ablation chamber, the particle crystal quality could be improved. Relatively low levels of crystallinity and secondary phases (even of different materials) are not, however, indicative of inferior properties.

Precisely the contrary has been found to be the case in recent experiments, in which HA particles of reduced crystallinity were found to exhibit bioactivity similar to surfaces functionalized with RGD peptides.

6.3 Summary of Results

XRD studies conducted on polydisperse HA nanoparticle substrates produced at synthesis temperatures between 850°C and 900°C showed evidence of diffraction by a material other than HA. At least one non-HA reflection was observed in an angular region where peaks for low-symmetry CaP materials are generally expected. Analysis at higher brilliance and resolution, after these samples were further annealed at 800°C for 1 hr, showed enhancement of these peaks and reasonable evidence that they can be asribed to the presence of the TTCP phase in the samples. The distortions observed in the TTCP lattice parameters, as compared to the relaxed structure, suggest that this phase may exist in the samples in close association with HA. Despite their different space groups, the unit cell dimensions of these two CaP phases allow for a variety of metric fits between their structures. Good chemical fits and possible topotactic transformations between the two structures also allow for the natural suggestion that TTCP might grow epitaxially on pre-existing HA crystallites under dehydroxylating conditions. Due to the small intensity of the observed TTCP reflections, quantification of the TTCP concentration relative to HA was not possible. Interaction of TTCP with CaO also present in some samples, which could lead to strain in TTCP, cannot be ruled out. CaO does appear to interact strongly with a fraction of the HA phase in the samples, leading to a compression of ~0.2% of the HA structure. Finally, further studies able to resolve the crystal phase domains within a single nanoparticle, or at least over the micron range, would be needed to ascertain whether the biphasic nature of the sample is due to biphasic nanoparticles per se, or to separate populations of HA and TTCP particles coexisting in the same sample. Despite these uncertainties, these findings suggest that it may be possible to use gas-phase laser methods to fabricate nanoparticle-based biphasic HA/TTCP particle ensembles that could be of interest in biomedicine, as they would combine the desirable mechanical stability of nonresorbable HA, with the enhanced bioactivity of the resorbable TTCP phase. This combination of properties is difficult to achieve in a single-phase material and could open new opportunities for nanostructured bioceramics research.

CHAPTER 7

SUMMARY AND CONCLUSIONS

This dissertation was devoted to the exploration of the synthesis and properties of CaP nanoparticles. Synthesis was performed by combination of the particle generation capabilities of laser-induced vaporization from microcrystalline HA in inert and reactive environments with several aerosol processing techniques. An experimental system was first developed to enable CaP nanoparticle fabrication by this approach. System development went through various iterations as a result of a growing understanding of the proposed techniques and the conditions needed for controlling CaP nanoparticle characteristics. TEM, AFM, XRD, and OA were used for physical characterization of particle samples deposited on surfaces and to a lesser extent suspended in solution.

Particles produced by laser ablation in inert and room-temperature environments were used to explore the range of morphologies achievable by the method. These particles were found to be amorphous from an atomic arrangement point of view. Compact spherical particles with average size ~100 nm are preferentially synthesized at low energy densities. At high energy densities these compact particles are accompanied by small aggregates (20-100 nm) with primary particles <10 nm. Changes in processing allow control of aggregation of both particle populations leading to samples dominated by fractal-like aggregates. These amorphous, complex-shaped nanophase aggregates might have interesting bioactivity and should allow stimulating studies in relation to cell behavior, particularly as it pertains to their kinetics of dissolution and interaction with cell membrane structures.

Laser synthesis in an OH-rich reactive environment with well controlled partial pressure of water vapor and temperature, followed by electrical mobility classification, led to aggregation-free, size-controlled HA nanoparticles. These particles exhibited narrow size distributions ($\sigma_g \approx 1.2$) typically with two well-resolved peaks with mean diameters below 100 nm, corresponding to singly and multiply charged particles. They were deposited on atomically flat, bioinert solid substrates in adjustable number concentrations, without appreciable aggregation upon deposition. Adsorption of E_7RGD-FITC peptides on polydisperse as well as size-controlled HA nanoparticle substrates was found to scale with particle concentration and may enable studies for decoupling the effects of nanotopography and biochemical cues in integrin-mediated cell adhesion. The particles were also found to be amenable to dispersion in water-based solutions, as monitored by OA experiments, which could significantly expand the applicability of the particles in biomedicine.

For synthesis temperatures above 850°C, nanoparticle samples showed evidence of formation of TTCP phase in addition to HA. Distortions observed in the TTCP lattice parameters suggest close crystallographic association with HA or with another non-CaP material found in the samples (CaO). These findings suggest that it may be possible to use laser gas-phase methods to fabricate nanostructured substrates with biphasic HA/TTCP configurations, which could be of interest in biomedicine, as they would combine the desirable mechanical stability of nonresorbable HA, with the enhanced bioactivity of the resorbable TTCP phase, a combination of properties that is difficult to achieve in a single-phase material. Much research is still needed to clarify the microstructure as well as kinetics of dissolution of such biphasic systems to assess their potential in terms of stability and bioactivity. However, the success of biphasic CaPs in the form of bulk ceramics and coatings over the past decade suggests that these biphasic nanophase materials could have significant impact in biomaterials research and create new applications for nanotechnology-based systems using the admittedly safe and bio-friendly CaP particles.

CHAPTER 8

FUTURE STUDIES

The main scope of this dissertation was to explore a new method for synthesizing CaP nanoparticles of controlled size, phase composition and controlled nanotopography on the Si substrates. The successful production of these CaP nanoparticles as well as successful attachment of biomolecules (E_7RGD-FITC) on CaP substrates demonstrated the ability of the synthesis method as well as the biocompatibility of the CaP substrates. In closing this dissertation, it is interesting to elaborate on the future work that we envision in this area. A variety of experiments could possibly improve the actual method as well as enable the study of integrin–mediated cell adhesion processes using the CaP substrates developed in this work.

As described in Section 5.6, we can successfully attach RGD peptides to polydisperse as well as size-controlled CaP nanoparticle substrates. Based on prior studies [88] the modification of RGD-FITC peptide using a polyglutamate sequence was used for attaching the peptides to the CaP substrates. However, the exact role played by the polyglutamate sequence in promoting better attachment to these substrates is unclear. Hence, a natural next step in these experiments would be to a polyglutamate sequence only (devoid of RGD) attached to the substrates as a control sample and compare its effect with E_7RGD-FITC conjugated substrates. Research studies pertaining to cell attachment on substrates with controlled nanotopography have shown that the disordered arrangement of RGD peptides increases the cell attachment as compared to the ordered arrangement [90, 131]. These studies have shown that the interparticle spacing between RGD-conjugated gold nanoparticles plays an important role in terms of cell attachment. A considerable amount of reduction is seen in cell adhesion and spreading if the distance between two peptides is more than 70 nm in length. While effective adhesion is observed if the distance is less than 58 nm. Even though we do not have control over particle ordering on the surfaces, adjusting the interparticle spacing is possible by increasing or reducing the number density of the particles. It would be interesting to see how the CaP nanotopography affects cell adhesion given the bioactive nature of CaP nanoparticles as opposed to the bioinert nature of gold nanoparticles used in the above mentioned research. Given the nature of these experiments; the size of the cells and the liquid medium, it is absolutely essential that the nanoparticles are firmly attached to the substrate. This attachment could be improved by functionalizing the substrates with chemical species that could promote covalent bonding between the depositing particles and surfaces. Given the possible biphasic nature of the substrates (as discussed in Chapter 6), it would also be interesting to study the dissolution behavior of these nanoparticles as that may play an important role in cell adhesion process. These experiments might also bring new insights to the understanding of integrin-mediated cell adhesion process.

CHAPTER 9

LIST OF PUBLICATIONS AND PRESENTATIONS

The work developed in this dissertation has been featured in the following publications and presentations. (In the case of conference presentations, underlined name indicates the name of the presenter):

- **Parimal V. Bapat**, Rebecca Kraft, Marco C. Bottino *and* Renato P. Camata, *"Nanoparticle-based Calcium Phosphate Substrates: Gas Phase Synthesis and Potential Applications"* in Biosurfaces and Biointerfaces, edited by J. A. Garrido, E. Johnston, C. Werner, T. Boland (Mater. Res. Soc. Symp. Proc. **1236E**, Warrendale, PA, 2009), 1236-SS08-51. *DOI: 10.1557/PROC-1236-SS08-51*.

- **Parimal V. Bapat**, Rebecca Kraft, *and* Renato P. Camata, *"Gas Phase Laser Synthesis of Aggregation-Free, Size-Controlled Hydroxyapatite Nanoparticles*," Scripta Materialia, *Submitted for publication.*

- **Parimal V. Bapat**, Bonnie K. Culpepper, Susan L. Bellis *and* Renato P. Camata *"Peptide Adsorption on Hydroxyapatite Nanoparticle-based Substrates with Controlled Nanotopography" Manuscript in preparation*.

- **Parimal V. Bapat** *and* Renato P. Camata

"Pulsed Laser Gas Phase Synthesis of Calcium Phosphate Nanoparticles" Manuscript in preparation.

- Rebecca Kraft, **Parimal V. Bapat**, Marco C. Bottino, Bradley Eaton, *and* Renato P. Camata, *"Nanoengineered Calcium Phosphate Substrates for Decoupling the Effects of Nanotopopraphy and Biochemical Cues in Integrin-Mediated Cell Adhesion,"* 2009 Fall Meeting of the Materials Research Society, November 30-December 4, 2009, Boston, Massachusetts.

- **Parimal V. Bapat**, Rebecca Kraft, Marco C. Bottino, *and* Renato P. Camata, *"Nanoparticle based Multifunctional Substrates for Controlling Integrin-mediated Cell Adhesion',"* 2010 Spring Meeting of the Materials Research Society, April 5-9, 2010, San Francisco, California.

- **Parimal V. Bapat** *and* R. P. Camata, *"Designer Hydroxyapatite Surfaces with Tunable Nanoscale Morphology for Controlling Integrin-Mediated Cell Adhesion,"* 2010 Fall Meeting of the Materials Research Society, November 29-December 3, 2010, Boston, Massachusetts.

- **Parimal V. Bapat** *and* Renato P. Camata, *"Aerosol Synthesis of Calcium Phosphate Nanoparticles for Applications in Medicine"* X Brazilian MRS Meeting 2011, September 25-29, 2011, Gramado, Rio Grande do Sul, Brazil.

- **Parimal V. Bapat** *and* Renato P. Camata, *"Gas Phase Synthesis of Calcium Phosphate Nanoparticles for Applications in Medicine"* 2nd Meeting of the Brazilian Association for Aerosol Research (BAAR 2011), August 1-5, 2011, Rio de Janeiro, Brazil.

LIST OF REFERENCES

[1] Hench LL. An Introduction to bioceramics. In: Wilson J, editor: World Scientific, 1983.
[2] Hench LL. BIOCERAMICS - FROM CONCEPT TO CLINIC. Journal of the American Ceramic Society 1991;74:1487.
[3] Hench LL. Bioceramics. Journal of the American Ceramic Society 1998;81:1705.
[4] B. Albert DB, J. Lewis, M. Raff, K. Roberts, J.Watson. Molecular Biology of the Cell. (Garland Publishing, 1994
[5] Giannoudis PV, Dinopoulos H, Tsiridis E. Bone substitutes: An update. Injury-International Journal of the Care of the Injured 2005;36:20.
[6] Paital SR, Dahotre NB. Calcium phosphate coatings for bio-implant applications: Materials, performance factors, and methodologies. Materials Science & Engineering R-Reports 2009;66:1.
[7] Sun LM, Berndt CC, Gross KA, Kucuk A. Material fundamentals and clinical performance of plasma-sprayed hydroxyapatite coatings: A review. Journal of Biomedical Materials Research 2001;58:570.
[8] Prabhakaran MP, Venugopal J, Ramakrishna S. Electrospun nanostructured scaffolds for bone tissue engineering. Acta Biomaterialia 2009;5:2884.
[9] Liao S, Wang W, Uo M, Ohkawa S, Akasaka T, Tamura K, Cui FZ, Watari F. A three-layered nano-carbonated hydroxyapatite/collagen/PLGA composite membrane for guided tissue regeneration. Biomaterials 2005;26:7564.
[10] Epple M, Ganesan K, Heumann R, Klesing J, Kovtun A, Neumann S, Sokolova V. Application of calcium phosphate nanoparticles in biomedicine. Journal of Materials Chemistry 2010;20:18.
[11] Ferraz MP, Mateus AY, Sousa JC, Monteiro FJ. Nanohydroxyapatite microspheres as delivery system for antibiotics: Release kinetics, antimicrobial activity, and interaction with osteoblasts. Journal of Biomedical Materials Research Part A 2007;81A:994.
[12] Ye F, Guo HF, Zhang HJ, He XL. Polymeric micelle-templated synthesis of hydroxyapatite hollow nanoparticles for a drug delivery system. Acta Biomaterialia 2010;6:2212.
[13] Guo Y, Shi DL, Lian J, Dong ZY, Wang W, Cho HS, Liu GK, Wang LM, Ewing RC. Quantum dot conjugated hydroxylapatite nanoparticles for in vivo imaging. Nanotechnology 2008;19.
[14] Daculsi G. Biphasic calcium phosphate concept applied to artificial bone, implant coating and injectable bone substitute. Biomaterials 1998;19:1473.
[15] Kim H, Camata RP, Vohra YK, Lacefield WR. Control of phase composition in hydroxyapatite/tetracalcium phosphate biphasic thin coatings for biomedical applications. Journal of Materials Science-Materials in Medicine 2005;16:961.

[16] Voet D, Voet JG. Biochemistry. John Wiley & Sons Inc., 1994.

[17] Alberts B, Johnson A, Lewis J, Raff M, Roberts K, Walter P. Molecular Biology of the Cell. New York: Garland Science, 2002.

[18] Kay MI, Young RA, Posner AS. Crystal structure of hydroxyapatite. Nature 1964;204:1050.

[19] Rulis P, Ouyang LZ, Ching WY. Electronic structure and bonding in calcium apatite crystals: Hydroxyapatite, fluorapatite, chlorapatite, and bromapatite (vol 70, art no 155104, 2004). Physical Review B 2004;70.

[20] Calderin L, Stott MJ, Rubio A. Electronic and crystallographic structure of apatites. Physical Review B 2003;67.

[21] *Mathew M*, *Schroeder LW*, *Dickens B*, *Brown WE*. The crystal structure of Ca3$(PO_4)_2$., vol. B33: Acta Crystallographica, 1977. p.1325.

[22] Yashima M, Sakai A, T. K, Hoshikawa A. Crystal structureanalysis of [b]-tricalcium phosphate Ca3(PO4)2 by neutron powderdiffraction., vol. 175: Journal of Solid State Chemistry, 2003. p.272.

[23] Dickens B, Brown WE, Kruger GJ, Stewart JM. $Ca_4(PO_4)_2O$, tetracalcium diphosphate monooxide. Crystal structure and relationships to $Ca_5(PO_4)_3OH$ and $K_3Na(SO_4)_2$. vol. B29: Acta Crystallographica, 1973. p.2046.

[24] Ramay HRR, Zhang M. Biphasic calcium phosphate nanocomposite porous scaffolds for load-bearing bone tissue engineering. Biomaterials 2004;25:5171.

[25] Brown WE, Smith JP, R. LJ, William FA. Octacalcium Phosphate and Hydroxyapatite: Crystallographic and Chemical Relations between Octacalcium Phosphate and Hydroxyapatite. vol. 196: Nature, 1962. p.1050.

[26] Kamakura S, Sasano Y, Shimizu T, Hatori K, Suzuki O, Kagayama M, Motegi K. Implanted octacalcium phosphate is more resorbable than β-tricalcium phosphate and hydroxyapatite. vol. 59: Journal of Biomedical Materials Research, 2001. p.29.

[27] Beevers C. The crystal structure of dicalcium phosphate dihydrate, $CaHPO_4$.2 H_20., vol. 11: Acta Crystallographica, 1958. p.273.

[28] MacLennan G, Beevers CA. The Crystal Structure of Dicalcium Phosphate, $CaHPO_4$., vol. 8: Acta Crystallographica, 1955. p.579.

[29] LeGeros RZ. Biodegradation and bioresorption of calcium phosphate ceramics. Clinical materials 1993;14:65.

[30] Wang LJ, Nancollas GH. Calcium Orthophosphates: Crystallization and Dissolution. Chemical Reviews 2008;108:4628.

[31] Dorozhkin SV. Amorphous calcium (ortho)phosphates. Acta Biomaterialia 2010;6:4457.

[32] Mateus AYP, Barrias CC, Ribeiro C, Ferraz MP, Monteiro FJ. Comparative study of nanohydroxyapatite microspheres for medical applications. Journal of Biomedical Materials Research Part A 2008;86A:483.

[33] Balasundaram G, Sato M, Webster TJ. Using hydroxyapatite nanoparticles and decreased crystallinity to promote osteoblast adhesion similar to functionalizing with RGD. Biomaterials 2006;27:2798.

[34] Beaux MF, McIlroy DN, Gustin KE. Utilization of solid nanomaterials for drug delivery. Expert Opinion on Drug Delivery 2008;5:725.

[35] Sokolova V, Epple M. Inorganic nanoparticles as carriers of nucleic acids into cells. Angewandte Chemie-International Edition 2008;47:1382.

[36] Kester M, Heakal Y, Fox T, Sharma A, Robertson GP, Morgan TT, Altinoglu EI, Tabakovic A, Parette MR, Rouse SM, Ruiz-Velasco V, Adair JH. Calcium Phosphate Nanocomposite Particles for In Vitro Imaging and Encapsulated Chemotherapeutic Drug Delivery to Cancer Cells. Nano Letters 2008;8:4116.

[37] Altinoglu EI, Russin TJ, Kaiser JM, Barth BM, Eklund PC, Kester M, Adair JH. Near-Infrared Emitting Fluorophore-Doped Calcium Phosphate Nanoparticles for In Vivo Imaging of Human Breast Cancer. Acs Nano 2008;2:2075.

[38] Cai YR, Tang RK. Calcium phosphate nanoparticles in biomineralization and biomaterials. Journal of Materials Chemistry 2008;18:3775.

[39] Liu HN, Yazici H, Ergun C, Webster TJ, Bermek H. An in vitro evaluation of the Ca/P ratio for the cytocompatibility of nano-to-micron particulate calcium phosphates for bone regeneration. Acta Biomaterialia 2008;4:1472.

[40] Ergun C, Liu HN, Webster TJ, Olcay E, Yilmaz S, Sahin FC. Increased osteoblast adhesion on nanoparticulate calcium phosphates with higher Ca/P ratios. Journal of Biomedical Materials Research Part A 2008;85A:236.

[41] Uskokovic V, Uskokovic DP. Nanosized hydroxyapatite and other calcium phosphates: Chemistry of formation and application as drug and gene delivery agents. Journal of Biomedical Materials Research Part B-Applied Biomaterials 2011;96B:152.

[42] Fathi MH, Hanifi A, Mortazavi V. Preparation and bioactivity evaluation of bone-like hydroxyapatite nanopowder. Journal of Materials Processing Technology 2008;202:536.

[43] Gopi D, Govindaraju KM, Victor CAP, Kavitha L, Rajendiran N. Spectroscopic investigations of nanohydroxyapatite powders synthesized by conventional and ultrasonic coupled sol-gel routes. Spectrochimica Acta Part a-Molecular and Biomolecular Spectroscopy 2008;70:1243.

[44] Welzel T, Meyer-Zaika W, Epple M. Continuous preparation of functionalised calcium phosphate nanoparticles with adjustable crystallinity. Chemical Communications 2004:1204.

[45] Park HJ, Dabhade VV, Kim K, Kim SR, Kwon WT, Kim Y. Hydrothermal synthesis of hydroxyapatite powders using alkyl ammonium bromides as surfactants. ASBM7: Advanced Biomaterials VII 2007;342-343:873.

[46] Sarda S, Heughebaert M, Lebugle A. Influence of the type of surfactant on the formation of calcium phosphate in organized molecular systems. Chemistry of Materials 1999;11:2722.

[47] Kong XD, Sun XD, Lu JB, Cui FZ. Mineralization of calcium phosphate in reverse microemulsion. Current Applied Physics 2005;5:519.

[48] Li H, Zhu MY, Li LH, Zhou CR. Processing of nanocrystalline hydroxyapatite particles via reverse microemulsions. Journal of Materials Science 2008;43:384.

[49] Singh S, Bhardwaj P, Singh V, Aggarwal S, Mandal UK. Synthesis of nanocrystalline calcium phosphate in microemulsion - effect of nature of surfactants. Journal of Colloid and Interface Science 2008;319:322.

[50] Wei K, Lai C, Wang YJ. Formation of monetite nanoparticles and nanofibers in reverse micelles. Journal of Materials Science 2007;42:5340.

[51] Lai C, Wang YJ, Wei K. Nucleation kinetics of calcium phosphate nanoparticles in reverse micelle solution. Colloids and Surfaces a-Physicochemical and Engineering Aspects 2008;315:268.

[52] Rusu VM, Ng CH, Wilke M, Tiersch B, Fratzl P, Peter MG. Size-controlled hydroxyapatite nanoparticles as self-organized organic-in organic composite materials. Biomaterials 2005;26:5414.

[53] Li JJ, Chen YP, Yin YJ, Yao FL, Yao KD. Modulation of nano-hydroxyapatite size via formation on chitosan-gelatin network film in situ. Biomaterials 2007;28:781.

[54] Schachschal S, Pich A, Adler HJ, Mx. Growth of hydroxyapatite nanocrystals on polymer particle surface. Colloid and Polymer Science 2007;285:1175.

[55] Schmidt HT, Ostafin AE. Liposome directed growth of calcium phosphate nanoshells. Advanced Materials 2002;14:532.

[56] Schmidt HT, Gray BL, Wingert PA, Ostafin AE. Assembly of aqueous-cored calcium phosphate nanoparticles for drug delivery. Chemistry of Materials 2004;16:4942.

[57] Tjandra W, Ravi P, Yao J, Tam KC. Synthesis of hollow spherical calcium phosphate nanoparticles using polymeric nanotemplates. Nanotechnology 2006;17:5988.

[58] Pretto M, Costa AL, Landi E, Tampieri A, Galassi C. Dispersing behavior of hydroxyapatite powders produced by wet-chemical synthesis. Journal of the American Ceramic Society 2003;86:1534.

[59] Bow JS, Liou SC, Chen SY. Structural characterization of room-temperature synthesized nano-sized beta-tricalcium phosphate. Biomaterials 2004;25:3155.

[60] Liou SC, Chen SY, Lee HY, Bow JS. Structural characterization of nano-sized calcium deficient apatite powders. Biomaterials 2004;25:189.

[61] Ethirajan A, Ziener U, Chuvilin A, Kaiser U, Colfen H, Landfester K. Biomimetic hydroxyapatite crystallization in gelatin nanoparticles synthesized using a miniemulsion process. Advanced Functional Materials 2008;18:2221.

[62] Wang J, Nonami T, Yubata K. Syntheses, structures and photophysical properties of iron containing hydroxyapatite prepared by a modified pseudo-body solution. Journal of Materials Science-Materials in Medicine 2008;19:2663.

[63] Marchi J, Greil P, Bressiani JC, Bressiani A, Muller F. Influence of Synthesis Conditions on the Characteristics of Biphasic Calcium Phosphate Powders. International Journal of Applied Ceramic Technology 2009;6:60.

[64] Loher S, Stark WJ, Maciejewski M, Baiker A, Pratsinis SE, Reichardt D, Maspero F, Krumeich F, Gunther D. Fluoro-apatite and calcium phosphate nanoparticles by flame synthesis. Chemistry of Materials 2005;17:36.

[65] Bisht S, Bhakta G, Mitra S, Maitra A. pDNA loaded calcium phosphate nanoparticles: highly efficient non-viral vector for gene delivery. International Journal of Pharmaceutics 2005;288:157.

[66] Doat A, Pelle F, Gardant N, Lebugle A. Synthesis of luminescent bioapatite nanoparticles for utilization as a biological probe. Journal of Solid State Chemistry 2004;177:1179.

[67] Seiler MP, Gottschalk S, Cerullo V, Ratnayake M, Mane VP, Clarke C, Palmer DJ, Ng P, Rooney CM, Lee B. Dendritic cell function after gene transfer with adenovirus-calcium phosphate co-precipitates. Molecular Therapy 2007;15:386.

[68] Pareta RA, Taylor E, Webster TJ. Increased osteoblast density in the presence of novel calcium phosphate coated magnetic nanoparticles. Nanotechnology 2008;19.

[69] Stayton PS, Drobny GP, Shaw WJ, Long JR, Gilbert M. Molecular recognition at the protein-hydroxyapatite interface. Critical Reviews in Oral Biology & Medicine 2003;14:370.

[70] Goobes G, Goobes R, Shaw WJ, Gibson JM, Long JR, Raghunathan V, Schueler-Furman O, Popham JM, Baker D, Campbell CT, Stayton PS, Drobny GP. The structure, dynamics, and energetics of protein adsorption - lessons learned from adsorption of statherin to hydroxyapatite. Magnetic Resonance in Chemistry 2007;45:S32.

[71] Butler WT. Structural and functional domains of osteopontin. Osteopontin: Role in Cell Signalling and Adhesion 1995;760:6.

[72] Bolander ME, Young MF, Fisher LW, Yamada Y, Termine JD. Osteonectin cDNA sequence reveals potential binding regions for calcium and hydroxyapatite and shows homologies with both a basement membrane protein (SPARC) and a serine proteinase inhibitor (ovomucoid). Proceedings of the National Academy of Sciences of the United States of America 1988;85:2919.

[73] Fujisawa R, Wada Y, Nodasaka Y, Kuboki Y. Acidic amino acid-rich sequences as binding sites of osteonectin to hydroxyapatite crystals. Biochimica Et Biophysica Acta-Protein Structure and Molecular Enzymology 1996;1292:53.

[74] Goldberg HA, Warner KJ, Li MC, Hunter GK. Binding of bone sialoprotein, osteopontin and synthetic polypeptides to hydroxyapatite. Connective Tissue Research 2001;42:25.

[75] Oldberg A, Franzen A, Heinegard D. The primary structure of a cell-binding bone sialoprotein. The Journal of biological chemistry 1988;263:19430.

[76] Sabsay B, Stetlerstevenson WG, Lechner JH, Veis A. Domain-structure and sequence distribution in dentin phosphophoryn. Biochemical Journal 1991;276:699.

[77] Fujisawa R, Mizuno M, Nodasaka Y, Kuboki Y. Attachment of osteoblastic cells to hydroxyapatite crystals by a synthetic peptide (Glu(7)-Pro-Arg-Gly-Asp-Thr) containing two functional sequences of bone sialoprotein. Matrix Biology 1997;16:21.

[78] Gilbert M, Giachelli CM, Stayton PS. Biomimetic peptides that engage specific integrindependent signaling pathways and bind to calcium phosphate surfaces. Journal of Biomedical Materials Research Part A 2003;67A:69.

[79] Gilbert M, Shaw WJ, Long JR, Nelson K, Drobny GP, Giachelli CM, Stayton PS. Chimeric peptides of statherin and osteopontin that bind hydroxyapatite and mediate cell adhesion. Journal of Biological Chemistry 2000;275:16213.

[80] Itoh D, Yoneda S, Kuroda S, Kondo H, Umezawa A, Ohya K, Ohyama T, Kasugai S. Enhancement of osteogenesis on hydroxyapatite surface coated with synthetic peptide (EEEEEEEPRGDT) in vitro. Journal of Biomedical Materials Research 2002;62:292.

[81] Roessler S, Born R, Scharnweber D, Worch H, Sewing A, Dard M. Biomimetic coatings functionalized with adhesion peptides for dental implants. Journal of Materials Science-Materials in Medicine 2001;12:871.

[82] Kasugai S, Fujisawa R, Waki Y, Miyamoto K, Ohya K. Selective drug delivery system to bone: Small peptide (Asp)(6) conjugation. 2000. p.936.

[83] Ruoslahti E. RGD and other recognition sequences for integrins. Annual Review of Cell and Developmental Biology 1996;12:697.

[84] Ruoslahti E. The RGD story: a personal account. Matrix Biology 2003;22:459.

[85] Gumbiner BM. Cell adhesion: The molecular basis of tissue architecture and morphogenesis. Cell 1996;84:345.

[86] Brown NH. Cell-cell adhesion via the ECM: integrin genetics in fly and worm. Matrix Biology 2000;19:191.

[87] Hynes RO. Integrins: Bidirectional, allosteric signaling machines. Cell 2002;110:673.

[88] Sawyer AA, Weeks DM, Kelpke SS, McCracken MS, Bellis SL. The effect of the addition of a polyglutamate motif to RGD on peptide tethering to hydroxyapatite and the promotion of mesenchymal stem cell adhesion. Biomaterials 2005;26:7046.

[89] Arnold M, Cavalcanti-Adam EA, Glass R, Blummel J, Eck W, Kantlehner M, Kessler H, Spatz JP. Activation of integrin function by nanopatterned adhesive interfaces. Chemphyschem 2004;5:383.

[90] Huang JH, Grater SV, Corbellinl F, Rinck S, Bock E, Kemkemer R, Kessler H, Ding JD, Spatz JP. Impact of Order and Disorder in RGD Nanopatterns on Cell Adhesion. Nano Letters 2009;9:1111.

[91] Thian ES, Ahmad Z, Huang J, Edirisinghe MJ, Jayasinghe SN, Ireland DC, Brooks RA, Rushton N, Bonfield W, Best SM. The role of electrosprayed apatite nanocrystals in guiding osteoblast behaviour. Biomaterials 2008;29:1833.

[92] Zhang Y, Venugopal JR, El-Turki A, Ramakrishna S, Su B, Lim CT. Electrospun biomimetic nanocomposite nanofibers of hydroxyapatite/chitosan for bone tissue engineering. Biomaterials 2008;29:4314.

[93] Ashok M, Kalkura SN, Sundaram NM, Arivuoli D. Growth and characterization of hydroxyapatite crystals by hydrothermal method. Journal of Materials Science-Materials in Medicine 2007;18:895.

[94] An GH, Wang HJ, Kim BH, Jeong YG, Choa YH. Fabrication and characterization of a hydroxyapatite nanopowder by ultrasonic spray pyrolysis with salt-assisted decomposition. Materials Science and Engineering a-Structural Materials Properties Microstructure and Processing 2007;449:821.

[95] Nasiri-Tabrizi B, Honarmandi P, Ebrahimi-Kahrizsangi R. Synthesis of nanosize single-crystal hydroxyapatite via mechanochemical method. Materials Letters 2009;63:543.

[96] Rhee SH. Synthesis of hydroxyapatite via mechanochemical treatment. Biomaterials 2002;23:1147.

[97] Ignjatovic NL, Ajdukovic ZR, Savic VP, Uskokovic DP. Size effect of calcium phosphate coated with poly-DL-lactide-co-glycolide on healing processes in bone reconstruction. Journal of Biomedical Materials Research Part B-Applied Biomaterials 2010;94B:108.

[98] Kim H, Camata RP, Lee S, Rohrer GS, Rollett AD, Bellis SL, Vohra YK. Calcium Phosphate Bioceramics With Tailored Crystallographic Texture For Controlling Cell Adhesion. In: Sheetz MP, Groves JT, Discher D, editors. Mechanotransduction and Engineered Cell-Surface Interactions, vol. BB.2.7. 925E, Warrendale, PA,: Mater. Res. Soc. Symp Proc, 2006.

[99] Kim H, Camata RP, Lee S, Rohrer GS, Rollett AD, Vohra YK. Crystallographic texture in pulsed laser deposited hydroxyapatite bioceramic coatings. Acta Materialia 2007;55:131.

[100] Boutinguiza M, Lusquinos E, Comesana R, Riveiro A, Quintero F, Pou J. Production of microscale particles from fish bone by gas flow assisted laser ablation. Applied Surface Science 2007;254:1264.

[101] Seifert W, Borgstrom M, Deppert K, Dick KA, Johansson J, Larsson MW, Martensson T, Skold N, Svensson CPT, Wacaser BA, Wallenberg LR, Samuelson L.

Growth of one-dimensional nanostructures in MOVPE. Journal of Crystal Growth 2004;272:211.

[102] Hulser TP, Wiggers H, Kruis FE, Lorke A. Nanostructured gas sensors and electrical characterization of deposited SnO2 nanoparticles in ambient gas atmosphere. Sensors and Actuators B-Chemical 2005;109:13.

[103] Deppert K, Bovin JO, Malm JO, Samuelson L. A new method to fabricate size-selected compound semiconductor nanocrystals: Aerotaxy. Journal of Crystal Growth 1996;169:13.

[104] McMurry PH. A review of atmospheric aerosol measurements. Atmospheric Environment 2000;34:1959.

[105] Camata RP, Atwater HA, Vahala KJ, Flagan RC. Size classification of silicon nanocrystals. Applied Physics Letters 1996;68:3162.

[106] Geohegan DB, Puretzky AA, Duscher G, Pennycook SJ. Time-resolved imaging of gas phase nanoparticle synthesis by laser ablation. Applied Physics Letters 1998;72:2987.

[107] Nichols WT, Malyavanatham G, Henneke DE, O'Brien DT, Becker MF, Keto JW. Bimodal nanoparticle size distributions produced by laser ablation of microparticles in aerosols. Journal of Nanoparticle Research 2002;4:423.

[108] Kim JT, Chang JS. Generation of metal oxide aerosol particles by a pulsed spark discharge technique. Journal of Electrostatics 2005;63:911.

[109] Magnusson MH, Deppert K, Malm JO, Bovin JO, Samuelson L. Size-selected gold nanoparticles by aerosol technology. Nanostructured Materials 1999;12:45.

[110] Nakaso K, Fujimoto T, Seto T, Shimada M, Okuyama K, Lunden MM. Size distribution change of titania nano-particle agglomerates generated by gas phase reaction, agglomeration, and sintering. Aerosol Science and Technology 2001;35:929.

[111] Camata RP, Atwater HA, Flagan RC. Space-charge effects in nanoparticle processing using the differential mobility analyzer. Journal of Aerosol Science 2001;32:583.

[112] Tartaj P, Gonzalez-Carreno T, Bomati-Miguel O, Serna CJ, Bonville P. Magnetic behavior of superparamagnetic Fe nanocrystals confined inside submicron-sized spherical silica particles. Physical Review B 2004;69.

[113] Ostraat ML, Brongersma M, Atwater HA, Flagan RC. Nanoengineered silicon/silicon dioxide nanoparticle heterostructures. Solid State Sciences 2005;7:882.

[114] Seinfeld JH. Atmospheric Chemistry and Physics of Air Pollution. New York: John Wiley & Sons, 1986. p.288.

[115] Gelbard F, Tambour Y, Seinfeld JH. Sectional representations for simulating aerosol dynamics
vol. 76: J. Colloidal Interface Sci, 1980. p.541.

[116] Glikman E, Kelson I, Doan NV, Tietze H. An optimized algorithm for molecular dynamics simulation of large-scale systems. Journal of Computational Physics 1996;124:85.

[117] Sun Z, Axelbaum RL, Huertas JI. Monte Carlo simulation of multicomponent aerosols undergoing simultaneous coagulation and condensation. Aerosol Science and Technology 2004;38:963.

[118] Knutson EO, Whitby KT. Aerosol Classification by Electric Mobility Apparatus, Theory, and Applications J. Aerosol Sci, 1975.

[119] Serra P, Morenza JL. Analysis of hydroxyapatite laser ablation plumes in a water atmosphere. Applied Physics a-Materials Science & Processing 1998;67:289.

[120] Serra P, Palau J, Varela M, Esteve J, Morenza JL. Characterization of hydroxyapatite laser-ablation plumes by fast intensified ccd imaging. Journal of Materials Research 1995;10:473.

[121] L. S. Handbook of Thin Films Materials. In: Nalwa HS, editor. Pulsed laser deposition of thin films: expectations and reality. New York: Academic Press, 2002.

[122] Fernandez-Pradas JM, Sardin G, Cleries L, Serra P, Ferrater C, Morenza JL. Deposition of hydroxyapatite thin films by excimer laser ablation. Thin Solid Films 1998;317:393.

[123] Tsai DH, Kim SH, Corrigan TD, Phaneuf RJ, Zachariah MR. Electrostatic-directed deposition of nanoparticles on a field generating substrate. Nanotechnology 2005;16:1856.

[124] Seto T, Kawakami Y, Suzuki N, Hirasawa M, Aya N. Laser synthesis of uniform silicon single nanodots. Nano Letters 2001;1:315.

[125] Winklmayr W, Reischl GP, Lindner AO, Berner A. A New Electromobility Spectrometer for the Measurement of Aerosol Size Distributions in the Size Range from 1 to 1000 nm. Journal of Aerosol Science 1991;22:289.

[126] Bohern C, Huffman D. *Absorption and scattering of light by small particles* Wiley-Interscience. .

[127] Miotello RKaA. Mechanisms of Pulsed laser sputtering," *Pulsed Laser Deposition of Thin Films*: Wiley, , 1994.

[128] de Groot K. Bioceramics of Calcium Phosphate. Boca Raton: CRC Press, 1983.

[129] Hench LL, Wilson J. An Introduction to Bioceramics. Singapore: World Scientific, 1993.

[130] de Araujo TS, Macedo ZS, de Oliveira PASC, Valerio MEG. Production and characterization of pure and Cr3+-doped hydroxyapatite for biomedical applications as fluorescent probes. Journal of Materials Science 2007;42:2236.

[131] Spatz JP. Activation of integrin function by nanopatterned adhesive interfaces. Abstracts of Papers of the American Chemical Society 2005;230:329.